Research in Astronomy and Astrophysics, 25:075003 (16pp), 2025 July https://doi.org/10.1088/1674-4527/add9da
CSTR: 32081.14.RAA.add9da

The Fraction of [C II] Emission Originating from Ionized Gas in Local Galaxies

Jiamin Liu[1,2], Yinghe Zhao (赵应和)[1,3], and Jin-Ming Bai[1]
[1] Yunnan Observatories, Chinese Academy of Sciences, Kunming 650216, China; zhaoyinghe@ynao.ac.cn
[2] University of Chinese Academy of Sciences, Beijing 100049, China
[3] State Key Laboratory of Radio Astronomy and Technology, National Astronomical Observatories, Chinese Academy of Sciences, Beijing 100101, China
Received 2025 April 25; revised 2025 May 13; accepted 2025 May 15; published 2025 June 10

Abstract

This paper presents a statistical study of the division of the [C II] 158 μm line into ionized and neutral components, using a new carbon-to-nitrogen abundance ratio, log(C/N) = 0.75, for a sample of 108 local galaxies. We investigate the correlation between the ionized-to-total [C II] ratio ($[C II]_{ionized}/[C II]_{total}$) and the far-infrared color $f60/f100$, finding a moderate negative correlation. Additionally, we explore the dependence of $[C II]_{ionized}/[C II]_{total}$ on various physical properties. We find that $[C II]_{ionized}/[C II]_{total}$ exhibits a weak negative correlation with the offset from the main sequence and a moderate negative correlation with the [O III]88 μm/[N II] 122 μm. Furthermore, no significant correlation with molecular gas mass is found. It shows a positive correlation with metallicity. Our results suggest that $[C II]_{ionized}/[C II]_{total}$ is influenced by the ionization parameter, star formation efficiency and metallicity.

Key words: ISM: lines and bands – galaxies: evolution – galaxies: star formation – infrared: ISM

1. Introduction

The interstellar medium (ISM) plays an important role in galactic evolution, acting as both the birthplace of stars and the repository of stellar feedback products. Its multiphase structure (McKee & Ostriker 1977; Ferrière 2001) is determined by thermal instability, supernova feedback, and the inflow of gas onto the galactic disk (e.g., Kritsuk & Norman 2002; Elmegreen & Scalo 2004; Ballesteros-Paredes et al. 2007; Elmegreen 2007; McKee & Ostriker 2007; Joung et al. 2009; Elmegreen & Burkert 2010; Seifried et al. 2011). Among the various phases of the ISM, the cold neutral medium ($T_k < 100$ K) provides the exclusive environments conducive to star formation (Kennicutt & Evans 2012).

Molecular clouds comprise cold neutral medium cores enveloped by atomic gas, with transition regions exhibiting molecular hydrogen and atomic carbon (van Dishoeck & Black 1988). These regions, known as photodissociation regions (PDRs; Hollenbach & Tielens 1999), are responsible for much of the galactic infrared line and continuum emission (Crawford et al. 1985; Stacey et al. 2010; Wolfire et al. 2022). The infrared emission originates when far-ultraviolet (FUV; 6–13.6 eV) photons from young massive stars (Hollenbach & Tielens 1999; Meijerink 2006) are absorbed by dust grains, heating the gas. Such thermal energy is then re-emitted through far-infrared (FIR) fine-structure lines, primarily [O I] 63 μm, [N II] 122 μm, [C II] 158 μm, and [N II] 205 μm, which are the dominant coolants in the neutral gas and can be as bright as 0.1%–1% of the total FIR luminosity.

Quantitative analyses of PDRs rely on diagnostic line ratios (e.g., ([C II]+[O I]63 μm)/FIR, [C II]/CO, [C I]/CO) to constrain radiation field intensity (G_0) and gas density (n_H) (Tielens & Hollenbach 1985a; Kaufman et al. 1999). These diagnostics provide crucial insights into the star formation efficiency. Owing to carbon's high abundance, its sub-Rydberg ionization potential enabling efficient excitation, and minimal dust attenuation at long wavelengths (Heiles 1994; Luhman et al. 1998), [C II] 158 μm ($^2P_{3/2}\rightarrow{}^2P_{1/2}$) is typically the brightest among fine-structure lines in star-forming galaxies. It accounts for approximately 0.1%∼1% of the total FIR luminosity (Stacey et al. 1991, 2010; Malhotra et al. 1997, 2001; Brauher et al. 2008; Carilli & Walter 2013; Sargsyan et al. 2014; Zhao et al. 2016c), although this fraction can drop to 0.1% in luminous galaxies or galaxies with intense star formation activity (Zhang et al. 2018). In addition, [C II] 158 μm is the main coolant in the ISM (Tielens & Hollenbach 1985a, 1985b; Wolfire et al. 1995, 2003). It serves as a key diagnostic for probing the physical properties of the ISM. For example, it acts as a reliable tracer of star formation rate (SFR) in galaxies (De Looze et al. 2014; Vallini et al. 2015; Zhang et al. 2018; Sutter et al. 2019), and a critical probe of CO-dark molecular gas, where H_2 remains abundant but CO emission is faint or absent (Pineda et al. 2013; Madden et al. 2020; Zhao et al. 2024).

However, the relatively low ionization potential of carbon (11.26 eV, below that of hydrogen at 13.6 eV) allows its presence across multiple phases of the ISM, including PDRs, cold atomic gas, low-density H II regions, and diffuse warm ionized media (Kaufman et al. 1999; Sutter et al. 2019). This ubiquity necessitates a careful decomposition of [C II] emission components when employing it as a diagnostic tool, particularly separating between neutral gas-dominated emission and ionized gas contributions (Zhang et al. 2018). De Looze et al. (2014) found a [C II]-SFR relation with a dispersion of 0.42 dex, while Sutter et al. (2019) demonstrated that the [C II] emission originating from neutral phases robustly correlates with SFR, with a scatter of 0.23 dex. In contrast, the ionized gas component exhibits a larger scatter of 0.33 dex. The star formation correlates well with gas content, including molecular gas and atomic gas (Kennicutt 1998; de los Reyes & Kennicutt 2019; Kennicutt & De Los Reyes 2021). However, de los Reyes & Kennicutt (2019) found no significant relationship between star formation surface density and atomic gas in normal and dwarf galaxies. Therefore, separating [C II] 158 μm emission from different phases may be important for quantitatively deriving molecular gas mass and SFR.

[C II] 158 μm emission is crucial for probing the physical conditions of star-forming gas, particularly in high-redshift galaxies where alternative emission lines are fainter (Carilli & Walter 2013). With the advent of the Herschel Space Observatory (hereafter Herschel; Pilbratt et al. 2010) and Atacama Large Millimeter/submillimeter Array (hereafter ALMA. Wootten & Thompson 2009), more and more high-redshift ($z \approx 3$–5.5) [C II] surveys appear (e.g., ALMA-SPT; Spilker et al. 2016), ALMA Large Program to Investigate C^+ at Early Times (ALPINE; Le Fèvre et al. 2020); Reionization Era Bright Emission Line Survey (REBELS; Bouwens et al. 2022); ALMA Spectroscopic Survey (ASPECS; Uzgil et al. 2021). Carniani et al. (2020) discovered the most distant [C II] 158 μm emission at $z \sim 9.1$.

Ultraluminous infrared galaxies (ULIRGs) and luminous infrared galaxies (LIRGs) are pivotal tracers of galaxy evolution, powered by dust-obscured starbursts and/or active galactic nuclei (AGNs) with total luminosity comparable to that of quasars (Sanders & Mirabel 1996). LIRGs cover a complete evolutionary sequence from isolated galaxies to late-stage mergers, with high SFRs and specific SFR (e.g., sSFR = SFR/$M_\star$), and bridge the population of main-sequence galaxies and starbursts (Díaz-Santos et al. 2013). Compared to ULIRGs, LIRGs generally show lower AGN contributions to their total luminosities (Veilleux et al. 2009; Petric et al. 2011; Alonso-Herrero et al. 2012), making them key laboratories for studying the connection between normal star-forming galaxies and extreme AGN-dominated systems (Sanders & Mirabel 1996). Multi-band observations, including infrared, submillimeter, and X-ray data, enable the separation of AGN and starburst contributions (Armus et al. 2007), while FIR spectroscopy (e.g., [C II], [O III]88 μm) reveals the chemical evolution and energy balance of the ISM (Sturm et al. 2011).

Cosmologically, high-redshift ($z \sim 1$–3) LIRGs dominate dust-obscured star formation (Berta et al. 2011; Magnelli et al. 2011), with their local analogs providing essential templates for interpreting high-redshift observations (Desai et al. 2007; Pope et al. 2008; Menéndez-Delmestre et al. 2009; Díaz-Santos et al. 2010; Stacey et al. 2010). Systematic studies of local LIRGs' ISM properties not only reveal extreme starbursts (SFR $> 100\,M_\odot\,\mathrm{yr}^{-1}$) with merger-driven morphological transitions (Hopkins et al. 2008), but also resolve feedback mechanism of LIRGs on star formation density (>50%, Caputi et al. 2007; Rodighiero et al. 2010; Madau & Dickinson 2014).

In summary, quantifying the phase resolved [C II] distribution in local galaxies, especially (U)LIRGs whose [C II] emission from ionized gas can reach 30%(Herrera-Camus et al. 2018a), establishes a critical benchmark for interpreting ISM conditions in high-redshift galaxies. While velocity-resolved observations allow for separating different [C II]-emitting components in the Milky Way (Pineda et al. 2014), such resolution is rarely achievable in extragalactic studies. Only a few nearby galaxies achieve sufficient velocity resolution in CO, H I, and fine-structure line profiles to separate multiphase ISM contributions (Lebouteiller et al. 2019; Okada et al. 2019; Tarantino et al. 2021). This resolution gap highlights the need for alternative separation methods such as using another two bright emission lines, [N II] 122 μm ($^3P_2 \rightarrow {}^3P_1$) and [N II] 205 μm ($^3P_1 \rightarrow {}^3P_0$).

Nitrogen has a higher ionization energy (14.53 eV) than hydrogen, restricting its presence only in ionized gas (Zhang et al. 2018). Moreover, [N II] 205 μm has similar ionization properties and a critical density in ionized regions to those of [C II] ($n_{\mathrm{crit}} \sim 46\,\mathrm{cm}^{-3}$, $T_e = 8000$ K). Therefore, it can be utilized to separate contributions of [C II] 158 μm emission from ionized and neutral gas (Oberst et al. 2006; Walter et al. 2009; Goldsmith et al. 2012; Goldsmith et al. 2015). However, the [N II] 205 μm line is generally unobservable for local galaxies and extragalactic objects, with only a limited number of detections by satellites prior to Herschel. Wright et al. (1991) demonstrated that in the Milky Way, the [N II] 122 μm and [N II] 205 μm emission lines are the second brightest in the far-infrared/submillimeter bands, aside from [C II], contributing approximately 0.05% of the total FIR luminosity. Similarly, Brauher et al. (2008), Zhao et al. (2013), and Zhao et al. (2016a) reported that in starbursts and normal star-forming galaxies, these emission lines account for roughly 0.1% of the total FIR luminosity.

Assumptions for carbon and nitrogen abundances are required to separate [C II] fractions from different phases (Oberst et al. 2006). Recent work by Berg et al. (2019) measured a nearly constant log(C/N) of approximately 0.75 across a range of metallicities in low-metallicity dwarf galaxies, suggesting a revised carbon-to-nitrogen abundance ratio. Another analysis of Micheva et al. (2022) demonstrated that the mean metallicity in the diffuse ionized gas (DIG) (8.48) is consistent with that in the H II regions (8.53) across all distances within inner regions ($D \lesssim 245''$), showing no significant difference between the two regions. These findings show an increase in carbon abundance, while the nitrogen abundance remains unchanged compared with Oberst et al. (2006).

Above all, [C II] emission from neutral gas is a critical diagnostic for determining radiation field strength and gas density in PDR models (Tielens & Hollenbach 1985a; Kaufman et al. 1999). It also provides a reliable tracer for SFR and molecular gas masses (De Looze et al. 2014; Vallini et al. 2015; Sutter et al. 2019; Madden et al. 2020; Zhao et al. 2024). Recently, Zhao et al. (2024) investigated the global correlation between [C II] and CO(1-0) emission to derive [C II]-to-H_2 conversion factors ($\alpha_{[C\,II]}$). However, their analysis did not account for the separating contributions of [C II] from neutral and ionized gas phases. Based on these, we recalculated the proportional distribution of [C II] and conducted a statistical analysis of its dependence on ISM properties across a diverse sample of galaxies, including LIRGs, ULIRGs, early-type galaxies (ETGs), Key Insights on Nearby Galaxies: a Far-Infrared Survey with Herschel (KINGFISH; Kennicutt et al. 2011), "Survey with Herschel of the ISM in Nearby Infrared Galaxies" (SHINING; PI Sturm), and AGNs. To examine the universality of our findings, we gathered observational data from high-redshift galaxies.

The paper is organized as follows: In Section 2, we present the Herschel spectroscopy of our sample and the ancillary observations used in this work. In Section 3, we discuss the relationship between the fractional contribution of [C II] 158 μm emission from ionized gas and physical properties in galaxies. The summary of the results and conclusions is given in Section 4.

2. Sample and Data

In this study, metallicity is defined as the gas-phase oxygen abundance, expressed as 12+log(O/H). All metallicity measurements were calibrated using the Pettini & Pagel (2004) (hereafter PP04) O3N2 method, which utilizes the [O III]λ5007/Hβ and [N II]λ6584/Hα line ratios. For values of 12+log(O/H) derived from alternative methods, we converted them to the PP04 O3N2 calibration (Kewley & Ellison 2008).

2.1. The GOALS Sample

The Great Observatories All-sky LIRG Survey (GOALS; Armus et al. 2009) has compiled a complete sample of nearby ($0.003 < z < 0.0918$) galaxies, encompassing the mostly of the 60 μm-band flux-limited IRAS Revised Bright Galaxy Sample (RBGS), including approximately 240 individual galaxies with $10^{10\sim12.3} L_\odot$ across 202 galaxy systems (comprising 180 LIRGs ($10^{11} L_\odot < L_{\rm TIR} < 10^{12} L_\odot$) and 22 ULIRGs ($L_{\rm TIR} > 10^{12} L_\odot$)). This survey spans the complete galaxy merger continuum: from isolated/disk galaxies or widely separated galaxy pairs to advanced mergers where galactic nuclei have merged (Haan et al. 2011; Kim et al. 2013; Stierwalt et al. 2013, 2014). Moreover, it covers the spectrum from main-sequence galaxies to starburst galaxies, with approximately 1/4–1/3 of GOALS galaxies classified as main-sequence galaxies (Díaz-Santos et al. 2013).

Until now, numerous endeavors have utilized multi-band data across various research domains. These data sets primarily originate from space-based facilities, encompassing GALEX UV data (Howell et al. 2010), HST optical and near-infrared imaging data (Haan et al. 2011; Kim et al. 2013), Chandra X-ray data (Iwasawa et al. 2011), Spitzer/IRS data (Díaz-Santos et al. 2010, 2011; Petric et al. 2011; Inami et al. 2013; Stierwalt et al. 2013, 2014), and PACS and SPIRE spectroscopic data of Herschel (Zhao et al. 2013; Zhao et al. 2016a; Díaz-Santos et al. 2017; Lu et al. 2017a). Additionally, VLA, CARMA, and ALMA, these ground-based observatories have been employed to observe GOALS samples (e.g., Murphy et al. 2013; Xu et al. 2014, 2015; Zhao et al. 2016b).

We collected observations of the [O III]88 μm, [C II], [N II] 122 μm, and [N II] 205 μm fine-structure lines from Lu et al. (2017a), Díaz-Santos et al. (2017), and Zhao et al. (2016a), along with FIR color data (f_{60}/f_{100}) of IRAS data. To balance the linear scale of the galaxies with the telescope time required to achieve the target sensitivity (see Lu et al. 2017a), we selected galaxies with IR flux ($F_{\rm IR}$) greater than 6.5×10^{-13} W m^{-2}. Finally, 58 galaxies are selected with all three lines ([C II], [N II] 122 μm, and [N II] 205 μm) detected, while three galaxies only have 3σ upper limit measurements. These fine-structure line observations were conducted using the PACS and SPIRE instruments onboard the Herschel Space Telescope.

In the final sample, CO(1-0) data were obtained for 31 galaxies from Jiao et al. (2017), 5 from Kamenetzky et al. (2016), 3 from Yamashita et al. (2017), 3 from Herrero-Illana et al. (2019), and 3 from Alatalo et al. (2024). For six galaxies without CO(1-0) data, the molecular gas mass was estimated using the [C II] luminosity according to Zhao et al. (2024). The data for the remaining five galaxies were adopted from Combes et al. (2009), Papadopoulos et al. (2011), González-Alfonso et al. (2015), and Montoya Arroyave et al. (2023). Additionally, for the three galaxies with only 3σ upper limits, the CO(1-0) data were taken from Jiao et al. (2017), Yamashita et al. (2017), and Gao et al. (2022).

We obtained metallicity measurements for 19 sources from Pérez-Díaz et al. (2024), who calculated the chemical abundances using fine-structure lines in the mid-to-far-infrared range (Fernández-Ontiveros et al. 2021). According to Zhao et al. (2024), who compared the metallicities of 30 sources measured in PP04 and IR-based methods, we added 0.1 dex to convert to PP04 O3N2 calibration. We collected the metallicities of some sources from Sánchez-Menguiano et al. (2017) and Spinoglio et al. (2022). The 12+log(O/H) values of UGC 3608 and NGC 2341 were obtained from Rupke et al. (2008) and converted to PP04 O3N2 adopting the calibration of Kewley & Ellison (2008). The other metallicities were derived from the integrated line fluxes in Kewley et al. (2001), Corbett et al. (2003), and Moustakas & Kennicutt (2006) using the PP04 O3N2 method. The SFRs are in the range of $10^1 \sim 10^2\,M_\odot\,\mathrm{yr}^{-1}$, and the stellar masses are in the range of $10^{10} \sim 10^{12}\,M_\odot$ adopted from Howell et al. (2010) and U et al. (2012).

2.2. ETG and KINGFISH Sample

This sample includes 30 early-type galaxies and the KINGFISH sample with [C II] 158 μm, [N II] 122 μm, and [N II] 205 μm detections and $F_{\mathrm{IR}} > 6.5 \times 10^{-13}\,\mathrm{W\,m^{-2}}$. The [C II] 158 μm, [N II] 122 μm, and [N II] 205 μm lines observed by Herschel PACS/SPIRE were collected from Lapham et al. (2017), and ten sources have [O III]88 μm measurements from Fernández-Ontiveros et al. (2016). The CO data for ten sources were adopted from Helfer et al. (2003), seven sources from Alatalo et al. (2013), two sources from Young et al. (2008), and two sources from Sorai et al. (2019). The others were adopted from Kohno et al. (2003), Sofue et al. (2003), Albrecht et al. (2004), Kuno et al. (2007), Baan et al. (2008), Tsai et al. (2009), Ali et al. (2018) and Cao (2018). The stellar masses were calculated using the K-band absolute magnitude given in Cappellari et al. (2011). We adopted a mass-to-light ratio of $M_\star/L_{\mathrm{K}} = 0.6$ (Bell et al. 2003) for a Kroupa initial mass function (IMF, Kroupa 2002). The SFRs were adopted from Davis et al. (2014) in the range of 0.01 to several $M_\odot\,\mathrm{yr}^{-1}$, except for NGC 2146, which has an SFR of 14.93 $M_\odot\,\mathrm{yr}^{-1}$. We also collected 12+log(O/H) measurements from Rémy-Ruyer et al. (2014) and converted them to PP04 O3N2 (Pettini & Pagel 2004) using the calibration in Kewley & Ellison (2008).

2.3. SHINING Sample

The SHINING sample comprises galaxies observed in six of the brightest PDR and H II region lines within the Herschel/PACS spectral range, specifically [C II] 158 μm, [O I] 145 μm, [O I]63 μm PDR lines, and [N II] 205 μm, [O III]88 μm, and [N III] H II region lines (Herrera-Camus et al. 2018a). We selected galaxies with detected [C II] 158 μm, [N II] 122 μmand [N II] 205 μm lines and $F_{\mathrm{IR}} > 6.5 \times 10^{-13}\,\mathrm{W\,m^{-2}}$. This selection resulted in eight galaxies, with [N II] 122 μm, [O III]88 μm, and [C II] 158 μm lines sourced from Herrera-Camus et al. (2018a) and [N II] 205 μm lines from Kamenetzky et al. (2014). The stellar masses of these galaxies range from 10^{10} to $10^{13}\,M_\odot$, and their SFRs span from several to $10^{1.6}\,M_\odot\,\mathrm{yr}^{-1}$. Metallicity measurements for three sources were taken from Pérez-Díaz et al. (2024) and converted to the PP04 O3N2 calibration by adding 0.1 dex. For the remaining sources, 12+log(O/H) values were obtained from Spinoglio et al. (2022) and Casasola et al. (2022).

2.4. AGN Sample

The AGN sample from Fernández-Ontiveros et al. (2016) was cross-matched with the previous samples to remove duplicate sources. Based on the selection criteria described earlier, 15 new sources were added. The 12+log(O/H) values for NGC 3031 and NGC 5194 were obtained from Pilyugin et al. (2004), while the metallicities for four sources were collected from Dors et al. (2015) and Spinoglio et al. (2022). The 12+log(O/H) for IRAS 23365+3604 was acquired from Rupke et al. (2008) and converted to the PP04 O3N2 using the calibration in Kewley & Ellison (2008). Additional metallicities sourced from Pérez-Díaz et al. (2021) and Pérez-Díaz et al. (2024) were converted to the PP04 O3N2 calibration by adding 0.1 dex. The CO data were collected from van Driel et al. (1991), Evans et al. (2002), Leroy et al. (2008), Papadopoulos et al. (2011), Xia et al. (2012), Esposito et al. (2022) and Montoya Arroyave et al. (2023), with stellar masses ranging from 10^{10} to $10^{12}\,M_\odot$ while their SFRs range from 0.1 to a few hundreds $M_\odot\,\mathrm{yr}^{-1}$ (Kang et al. 2015; Cullen et al. 2019; George et al. 2019; Esposito et al. 2022; Farrah et al. 2022; Vinod et al. 2023; Graham et al. 2024; Nandi & Subramonian Stalin 2024).

2.5. High-Redshift Galaxies

Of the 10 high-redshift ($z > 4$) galaxies in our sample with both [C II] and [N II] 205 μm measurements, three exhibit [N II] 122 μm detections (including a 3σ upper limit for SPT0346-52). Molecular gas masses were calculated from CO transition lines using a (U)LIRGs calibrated α_{CO} conversion factor. For CO(2-1) emission, we adopted $R_{21} = \mathrm{I(CO(2\text{–}1))/I(CO(1\text{–}0))} = 0.85$. SFRs and stellar masses were gathered from previous studies (Solomon & Vanden Bout 2005; Gilli et al. 2014; Ma et al. 2015; Yun et al. 2015; Lu et al. 2017b; Cheng et al. 2020; Jones et al. 2020; Dye et al. 2022; Tripodi et al. 2022; Salak et al. 2024; Sun et al. 2024).

3. Results and Discussion

3.1. [C II] 158 μm Emission

The emission of [C II] 158 μm arises from both ionized gas and PDRs due to the differing ionization potentials between carbon (11.26 eV) and hydrogen (13.6 eV). At a temperature of $T = 8000$ K, when ionized carbon is excited through collisions with free electrons or protons, the de-excitation density reaches approximately $44\,\mathrm{cm}^{-3}$ (Goldsmith et al. 2012), enabling rapid thermalization of the [C II] 158 μm line within moderately dense ionized environments. In summary, in galaxies with active star formation, the primary source of [C II] emission is the dense PDRs enveloping young, massive stars, where excitation of [C II] occurs via collisions with neutral and molecular hydrogen (Tielens & Hollenbach 1985a; Kaufman et al. 1999). The emission mechanisms of [C II] in H II regions and PDRs are influenced by several factors, such as the density and temperature of the gas, the presence of dust grains, and the intensity of the radiation field (Abel et al. 2005). In PDRs, photoelectric heating from dust grains plays a significant role in the excitation of C^+ (Weingartner & Draine 2001; Wolfire et al. 2003), while in H II regions, the contribution is more from the direct ionization by high-energy photons (Rubin 1985; Goldsmith et al. 2012). These variations in emission mechanisms reflect the intricate interplay between the physical conditions and the ambient radiation field in these regions.

3.1.1. [C II] 158 μm Arises from PDRs

The fine-structure lines of nitrogen can be categorized into [N II] 122 μm and [N II] 205 μm based on distinct energy level transitions. Notably, the critical density of [N II] 205 μm is close to that of [C II] ($n_{\rm crit} \sim 46\,{\rm cm}^{-3}$, $T_e = 8000$ K), implying analogous excitation conditions. The ionization energy of nitrogen atoms (14.53 eV) is close to that of carbon but arises only in the ionization region. Additionally, ionization potentials required to get to the next ionization state are close for [C II] and [N II] 205 μm, 24.38 eV and 29.60 eV, respectively. Thus, we can use [N II] 205 μm to estimate the fraction of [C II] arising from the ionized gas (Oberst et al. 2006; Zhang et al. 2018).

As mentioned in Oberst et al. (2006), the line ratio of [N II] 205 μm to [C II] 158 μm in the ionized gas depends solely on the abundance ratio of N^+/C^+. At temperature $T = 8000$ K, the carbon gas-phase abundance they adopted is $n(C^+)/n_e = 1.4 \times 10^{-4}$ while the nitrogen gas-phase abundance is $n(N^+)/n_e = 7.9 \times 10^{-5}$ (Savage & Sembach 1996). This implies a gas-phase abundance ratio of $\textbf{log}(C^+/N^+)= \log(1.4 \times 10^{-4}/7.9 \times 10^{-5}) \approx 0.25$. They corrected the fraction of the two elements expected in the first ionization state using the H II region models from Rubin (1985). Furthermore, in cool diffuse clouds, Savage & Sembach (1996) derived $\log(C/H) = -3.86$ and $\log(N/H) = -4.10$, leading to $\log(C/N) = \log(C/H)–\log(N/H) = 0.24$. Thus, we adopt log $(C/N) = 0.24$ to calculate the fraction of [C II] originating from ionized gas following the method of Oberst et al. (2006). As demonstrated by Berg et al. (2019), a larger constant value of carbon-to-nitrogen abundance ratio is derived in low-metallicity galaxies, $\log(C/N) = 0.75$ with 0.2 dex scatter. Adopting the solar metallicity of $12+\log(O/H) = 8.69$ (Asplund et al. 2009), we obtain $\log(C/N) = 0.9$. This value falls within the reported scatter, and the sample size is small at this metallicity. Consequently, we have adopted two carbon-to-nitrogen abundance ratios, $\log(C/N) = 0.75$ and $\log(C/N) = 0.24$, to estimate the proportion of [C II] 158 μm originating from the ionized gas, utilizing the method outlined by Oberst et al. (2006). This method computes the theoretical line ratios of [C II] 158 μm, [N II] 122 μm and [N II] 205 μm as a function of the electron density. Since the critical densities of [N II] 205 μm and [N II] 122 μm are 44 and 293 ${\rm cm}^{-3}$, respectively, the electron density of our sample can be inferred from the observed [N II] 122 μm/[N II] 205 μm ratio as illustrated in Figure 1.

Most of the 108 galaxies in our sample with line flux measurements (excluding upper limits) have electron densities in the range $10 \sim 100\,{\rm cm}^{-3}$. The median electron density for GOALS and the total sample are 32 and 23 ${\rm cm}^{-3}$ (corresponding [N II] 122 μm/[N II] 205 μm ratios are 1.53 and 1.27), respectively. The average n_e are 44 and 43 ${\rm cm}^{-3}$ (corresponding [N II] 122 μm/[N II] 205 μm = 1.8), respectively. This median line ratio for the total sample matches the value found by Zhao et al. (2016a) for a sample of 12 (U)LIRGs, while the GOALS shows a higher ratio. This suggests that the density of the ionized medium in our sample is relatively high and [N II] 205 μm emission is dominated by the low-density ionized gas.

Draine (2011) shows that the ionization parameter U is almost proportional to the density, so the ionization parameter in the high-density region is also high. Most N^+ is likely ionized to N^{++} (Abel et al. 2009; Fischer et al. 2014), and UV photons in dense environments are also efficiently absorbed by dust grains (Voit 1992; Bottorff et al. 1998; Draine 2011). The [N II]205 μm emission in the high-density region will be significantly reduced. So the [N II]205 μm emission of our sample should mostly come from the low-density regions that surround the dense regions (Xu et al. 2014, 2015).

The method described in Oberst et al. (2006), Goldsmith et al. (2012), and Goldsmith et al. (2015) was employed to derive the $[C\,II]_{\rm ionized}$/[N II] 205 μm ratio based on the n_e. This ratio is then utilized to calculate the [C II] 158 μm arising from the ionized gas, which is subsequently subtracted to determine the contribution of [C II] 158 μm from neutral gas. The uncertainty is calculated by a Monte Carlo (MC) simulation as follows. First, we generate a [N II] 122 μm/[N II] 205 μm ratio depending on the observational data and errors. Second, we calculate the $[C\,II]_{\rm ionized}$/[N II] 205 μm ratio using the generated [N II] 122 μm/[N II] 205 μm ratio. Finally, we calculate the standard deviation of the $[C\,II]_{\rm ionized}$/[N II] 205 μm ratios as the uncertainty after repeating the previous steps 10,000 times.

Figure 2 shows the fraction of [C II] 158 μm originating from PDRs as a function of galaxy FIR color, f_{60}/f_{100}. The dashed and solid lines show the trends. It is evident that the $[C\,II]_{\rm neutral}$ increases with increasing FIR color of the galaxy. For the GOALS sample, the Spearman correlation coefficient, which is a non-parametric measure of the monotonic relationship of two variables, between $[C\,II]_{\rm neutral}/[C\,II]_{\rm Total}$ and f_{60}/f_{100} is calculated. Adopting the two different carbon-to-nitrogen abundance ratios, the Spearman correlation coefficients are both 0.374, and the associated P-values for the null hypothesis of no monotonic relationship are 0.005 (<0.05). This suggests a moderate positive correlation between $[C\,II]_{\rm neutral}/[C\,II]_{\rm total}$ and f_{60}/f_{100}. However, the two variables have a stronger correlation for the full sample, with a Spearman correlation coefficient of 0.5 and a P-value of 3.8×10^{-8}.

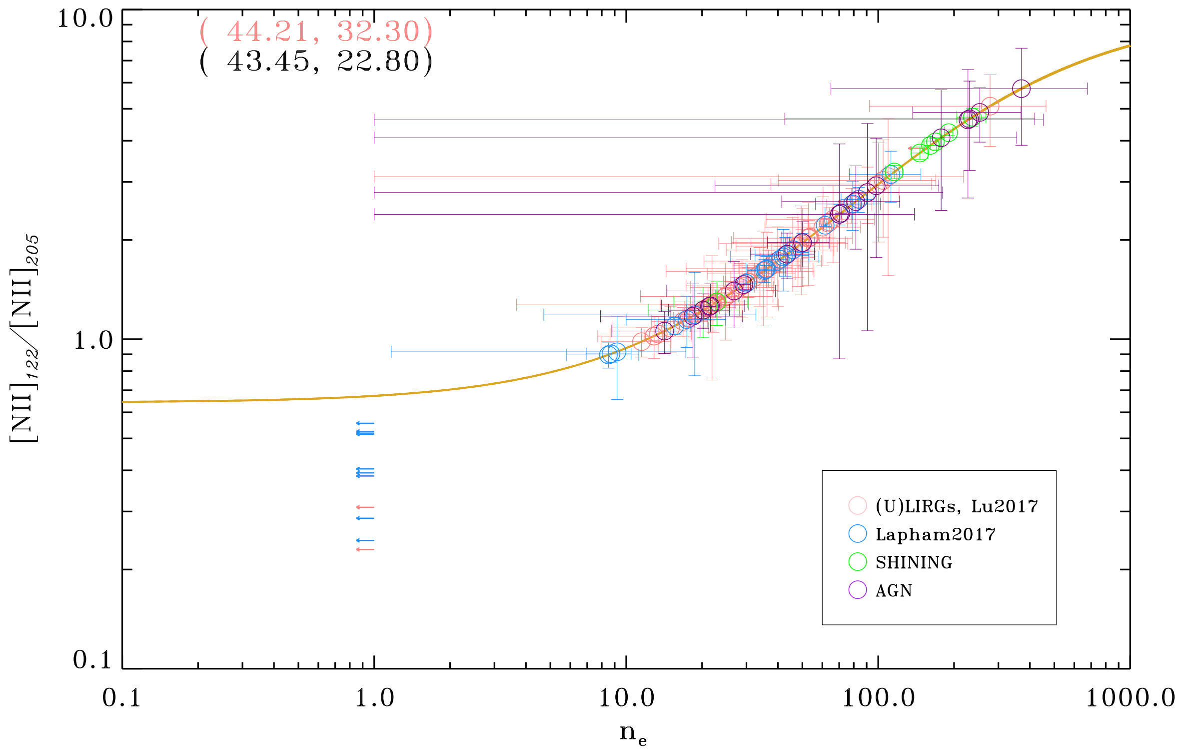

Figure 1. Line ratio of [N II] 122 μm to [N II] 205 μm as a function of electron density, n_e, for our sample. Colors denote different subsamples, as shown in the legend. The golden solid line indicates the theoretical ratio from Oberst et al. (2006). Most sources fall within 10∼100 cm^{-3}. The mean value is 43 cm^{-3} and median is 23 cm^{-3}. The arrows mean the densities below 1 cm^{-3}. The mean and median densities for GOALS and the total sample are indicated in pink and black, respectively.

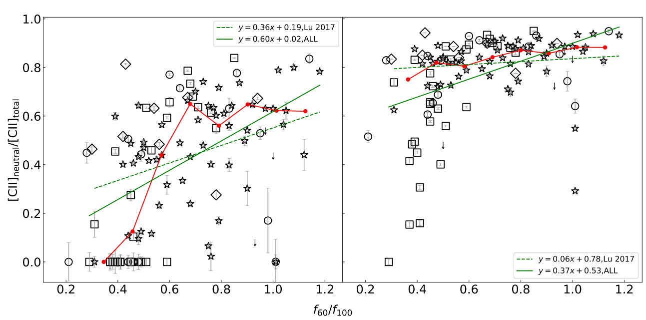

Figure 2. The fraction of [C II] arising from PDRs as a function of the f_{60}/f_{100} for our sample. The left panel shows the derived [C II] fraction from PDRs based on the Oberst et al. (2006) model, assuming a carbon-to-nitrogen abundance ratio of log(C/N) = 0.75. The right panel presents a similar plot, but with a different log(C/N) value of 0.24. In both panels, the stars represent (U)LIRGs as outlined in Lu et al. (2017a), the squares denote the ETGs and KINGFISH sample mentioned in Section 2, the diamonds represent the SHINING sample, and the open circles indicate AGNs. Arrows indicate lower limits on the fraction of [C II] arising from PDRs. Each data point includes error bars calculated using the MC method. The red points and lines in the left and right panels represent the median values in each f_{60}/f_{100} bin for the total sample and (U)LIRGs, respectively.

The [C II] 158 μm emission from PDRs decreases as the C/N increases. This is primarily attributable to the method used to calculate [C II]$_{\rm ionized}$/[N II] 205 μm. The electron density is derived from the two nitrogen emission lines, [N II] 122 μm and [N II] 205 μm, independent of abundance due to the same chemical element and ionization state. Consequently, the derived electron density remains essentially unchanged. However, the theoretical [C II]$_{\rm ionized}$/[N II] 205 μm ratio is correlated with the electron density and the carbon-to-nitrogen abundance ratio (Zhang et al. 2018), so the [C II] 158 μm/[N II] 205 μm is higher than adopting log(C/N) = 0.24.

3.1.2. *[C II] Arises from Ionized Gas*

Figure 3 presents a histogram illustrating the fraction of [C II] arising from the ionized gas. The dashed line indicates the total sample, while the colored and bordered regions represent subsamples with log(C/N) = 0.24 and 0.75, respectively. Note that for sources where [C II]$_{\rm ionized}$/[C II]$_{\rm total}$ exceeds 1, we take the value equal 1. At log(C/N) is 0.75, the GOALS subsample exhibits a mean and median [C II]$_{\rm ionized}$/[C II]$_{\rm total}$ of 55% and 51%, respectively, while the corresponding values for the total sample are 60% and 53%, respectively. Correspondingly, for log(C/N) = 0.24, the mean and median values are 18% and 15%, and 23% and 16% for the total sample, respectively. It is evident that [C II]$_{\rm ionized}$/[C II]$_{\rm total}$ increases approximately threefold at log (C/N) = 0.75, primarily due to a threefold increase in carbon-to-nitrogen abundance ratio ($10^{0.75}/10^{0.24}$ = 3.24).

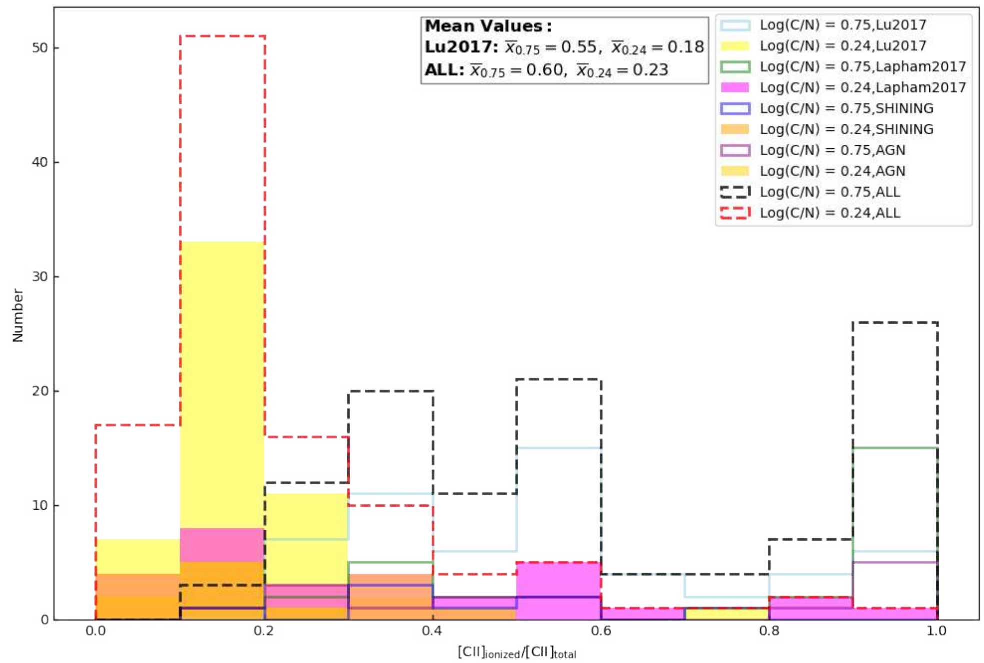

Figure 3. Histogram shows the fraction of [C II] emission arising from the ionized gas. The filled regions represent fractions calculated by the model from Oberst et al. (2006) with a carbon-to-nitrogen abundance ratio of 0.24, while the bordered areas represent results for $\log(C/N) = 0.75$. The red dashed line indicates the distribution of the total sample for $\log(C/N) = 0.24$, and the black dashed line represents the distribution for $\log(C/N) = 0.75$.

As shown in Figure 4, the fraction of [C II] originating from ionized gas exhibits a trend with f_{60}/f_{100}. The absolute value of the Spearman correlation coefficient and P-value are identical to those presented in Figure 2. In contrast to the $[\text{C II}]_{\text{neutral}}$, the proportion of ionized carbon ($[\text{C II}]_{\text{ionized}}$) decreases with increasing FIR color. This phenomenon may be attributed to the enhanced ionization of C^+ to higher ionization states (e.g., C^{++}) in environments with higher FIR color, indicative of more intense radiation fields. We will discuss this in the following sections.

3.2. The Effect of *Δ(MS)*

AGNs are usually observed in (U)LIRGs (Petric et al. 2011; Alonso-Herrero et al. 2012). To explain the trend mentioned above, the fraction of [C II] emission from ionized gas decreases as the FIR color f_{60}/f_{100} increases; we first consider the AGN contribution. Díaz-Santos et al. (2013, 2017) have shown that despite the prevalence of AGNs in numerous GOALS sources, the contribution of mid-infrared emission or photometric AGNs is minimal based on Spitzer/IRS spectrum diagnostic and 6.2 μm PAH equivalent width diagnostic analysis. Herrera-Camus et al. (2018b) also found [C II] emission is unaffected by AGNs in 12 ULIRGs. Consequently, the fine-structure lines are not significantly influenced by AGNs.

In general, the f_{60}/f_{100} serves as an indicator of dust temperature, which is closely linked to the physical conditions in star-forming (SF) regions within galaxies. Morokuma-

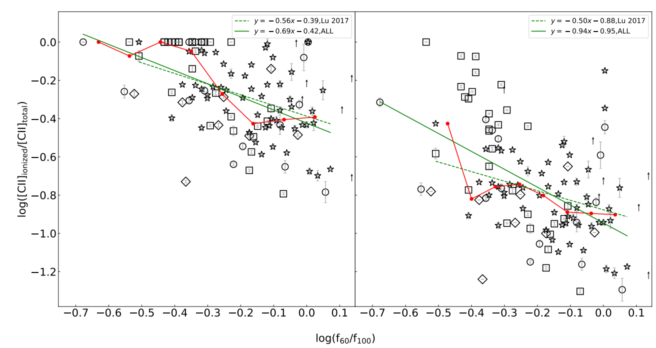

Figure 4. The proportion of [C II] arising from ionized gas as a function of the f_{60}/f_{100} for our sample. The symbols are the same as in Figure 2. Both axes are shown on a logarithmic scale.

Matsui et al. (2020) found a strong correlation between f_{60}/f_{100} and specific star formation rate ($\text{sSFR} = \text{SFR}/M_{\star}$), which is attributed to the intense ultraviolet (UV) radiation emitted by young, massive stars (Magnelli et al. 2014; Matsuki et al. 2017). In such environments, radiation from these young, hot stars heats the surrounding dust, enhancing infrared radiation at shorter wavelengths. UV photons from these stars heat the surrounding dust, which emits thermal infrared radiation. Therefore, the decrease of $[\text{C II}]_{\text{ionized}}$ portion may be caused by the stronger star formation activity. In these regions, the stronger radiation fields could ionize C^+ further to C^{++}, reducing the observed $[\text{C II}]_{\text{ionized}}$ emission.

To investigate the effect of SF, we utilize ΔMS defined by Accurso et al. (2017). ΔMS is the offset from the SF main sequence, which explains the SFR-Stellar mass relationship for SF galaxies and is recognized both in the local and distant universe. Here, the offset from the main sequence is defined as follows:

$$\Delta(\mathrm{MS}) = \log \frac{\mathrm{sSFR}}{\mathrm{sSFR_{MS}}} \tag{1}$$

with sSFR and $\mathrm{sSFR_{MS}}$ denoting the specific star formation rate of the galaxy and the main-sequence galaxies, respectively. The expression for $\mathrm{sSFR_{MS}}$ is given by Whitaker et al. (2012):

$$\begin{aligned} &\log(\mathrm{sSFR_{ms}}(z, M_*)) \\ &= -1.12 + 1.14z - 0.19z^2 - (0.3 + 0.13z) \\ &\times (\log M_* - 10.5)\,[\mathrm{Gyr}^{-1}], \end{aligned} \tag{2}$$

where z is the redshift and M_* is the stellar mass of the galaxy.

In this study, we analyze the Spearman correlation between f_{60}/f_{100} and Δ(MS) as shown in the top panel of Figure 5. For the GOALS sample and a total of 108 sources, their ρ values were 0.755 and 0.741, respectively, with corresponding p-values of 2.71×10^{-11} and 4.60×10^{-20}. These results indicate a strong positive correlation between them. This finding aligns with the observations reported by Magnelli et al. (2014) and Matsuki et al. (2017), who reported a strong positive correlation between dust temperature, as characterized by different tracers, and Δ(MS). Additionally, Morokuma-Matsui et al. (2020) also found a strong positive correlation between sSFR and f_{60}/f_{100} for the COMING sample. The strong positive correlation can be adequately explained by the premise that higher values of Δ(MS) imply higher radiative energy and sSFR (Magnelli et al. 2014). Furthermore, UV radiation is known to heat the surrounding dust, thereby resulting in galaxies with higher Δ(MS) exhibiting higher dust temperatures.

In addition, the Spearman correlation and Kendall rank correlation between $[\mathrm{C\,II}]_{\mathrm{ionized}}/[\mathrm{C\,II}]_{\mathrm{total}}$ and Δ(MS) are calculated. The Kendall's τ correlation coefficients were determined using the *cenken* function of the *NADA* package in the R software.[4] The Spearman correlation coefficients ρ and p-values are -0.224 and 0.1 for the GOALS sample, and -0.312 and 0.001 for the total sample. The Kendall correlation coefficients τ and p-values are -0.15 and 0.1 for the GOALS sample, and -0.19 and 0.004 for the total sample. Overall, there is a weak negative correlation between $[\mathrm{C\,II}]_{\mathrm{ionized}}/[\mathrm{C\,II}]_{\mathrm{total}}$ and Δ(MS) for the total sample, while no significant correlation is observed for the GOALS sample. This discrepancy may be attributed to the fact that the Δ(MS) of the GOALS sample is concentrated between 0.5 and 2, whereas the total sample covers a broader range, as displayed in Figure 5.

The bottom panel in Figure 5 shows the $[\mathrm{C\,II}]_{\mathrm{ionized}}/[\mathrm{C\,II}]_{\mathrm{total}}$ as a function of Δ(MS). As illustrated in figure, the $[\mathrm{C\,II}]_{\mathrm{ionized}}/[\mathrm{C\,II}]_{\mathrm{total}}$ exhibits a decline as Δ(MS) increases. High-redshift galaxies, represented by blue filled triangles in Figure 5, consistently follow this trend. For high-redshift galaxies, we calculate $[\mathrm{C\,II}]_{\mathrm{ionized}}/[\mathrm{C\,II}]_{\mathrm{total}}$ adopt [N II] 122 μm/[N II] 205 μm ratio of 2.2, based on the median value of the total sample. This finding supports the conclusions of Herrera-Camus et al. (2018a), who determined that the majority of [C II] 158 μm originates from neutral gas, and this proportion increases in most active SF regions. The increasing pressures in H II regions can potentially suppress [C II] 158 μm and [N II] 205 μm emission, and [C II] 158 μm emission from neutral gas appears less sensitive to this effect (Croxall et al. 2017).

Furthermore, previous studies have established that Δ(MS) is related to the UV radiation field (Zhao et al. 2024). This suggests the possibility of a connection between $[\mathrm{C\,II}]_{\mathrm{ionized}}/[\mathrm{C\,II}]_{\mathrm{total}}$ and the intensity of the radiation field. To explore this hypothesis, we utilize [O III]88 μm//[N II] 122 μm to examine the relationship between the radiation field strength and $[\mathrm{C\,II}]_{\mathrm{ionized}}/[\mathrm{C\,II}]_{\mathrm{total}}$ in the following section.

3.3. The Effect of Radiation Field

The [O III]88 μm/[N II] 205 μm ratio has been identified as an indicator of the hardness of the radiation field. However, it is essential to note that this ratio is sensitive to the electron density (Rubin 1985), given the significant difference in the critical densities of the two emission lines (Zhao et al. 2016a). Consequently, the ratio of [O III]88 μm and [N II] 122 μm, with comparable critical densities ($\sim$300 and $\sim$500 cm^{-3}, respectively) but distinct ionization potentials ($\sim$35.1 eV and $\sim$14.5 eV, respectively), is utilized as an indicator of the hardness of the radiation fields (Ferkinhoff et al. 2011; Zhang et al. 2018) for further analysis of the radiation field effect. We plot the observed [O III]88 μm/[N II] 122 μm for 79 sources as a function of FIR color in the top panel of Figure 6. The Spearman coefficients and p-values are 0.313 and 0.02 for GOALS, and 0.391 and 0.0004 for the total sample, respectively. The best-fit linear regression is shown in the top-left corner of the panel. These results indicate a moderate positive correlation between the [O III]88 μm/[N II] 122 μm and FIR color, consistent with the study of Δ(MS) in Section 3.2.

The $\log([\mathrm{C\,II}]_{\mathrm{ionized}}/[\mathrm{C\,II}]_{\mathrm{total}})$ is plotted as a function of log ([O III]88 μm/[N II] 122 μm) in the bottom panel of Figure 6. Red filled circles and connecting lines represent the median values in different [O III]88 μm/[N II] 122 μm bins, indicating a decreasing trend of $[\mathrm{C\,II}]_{\mathrm{ionized}}/[\mathrm{C\,II}]_{\mathrm{total}}$ with increasing [O III]88 μm/[N II] 122 μm. It is evident that, different from the Δ(MS) analysis, the [O III]88 μm/[N II] 122 μm

[4] http://www.R-project.org/

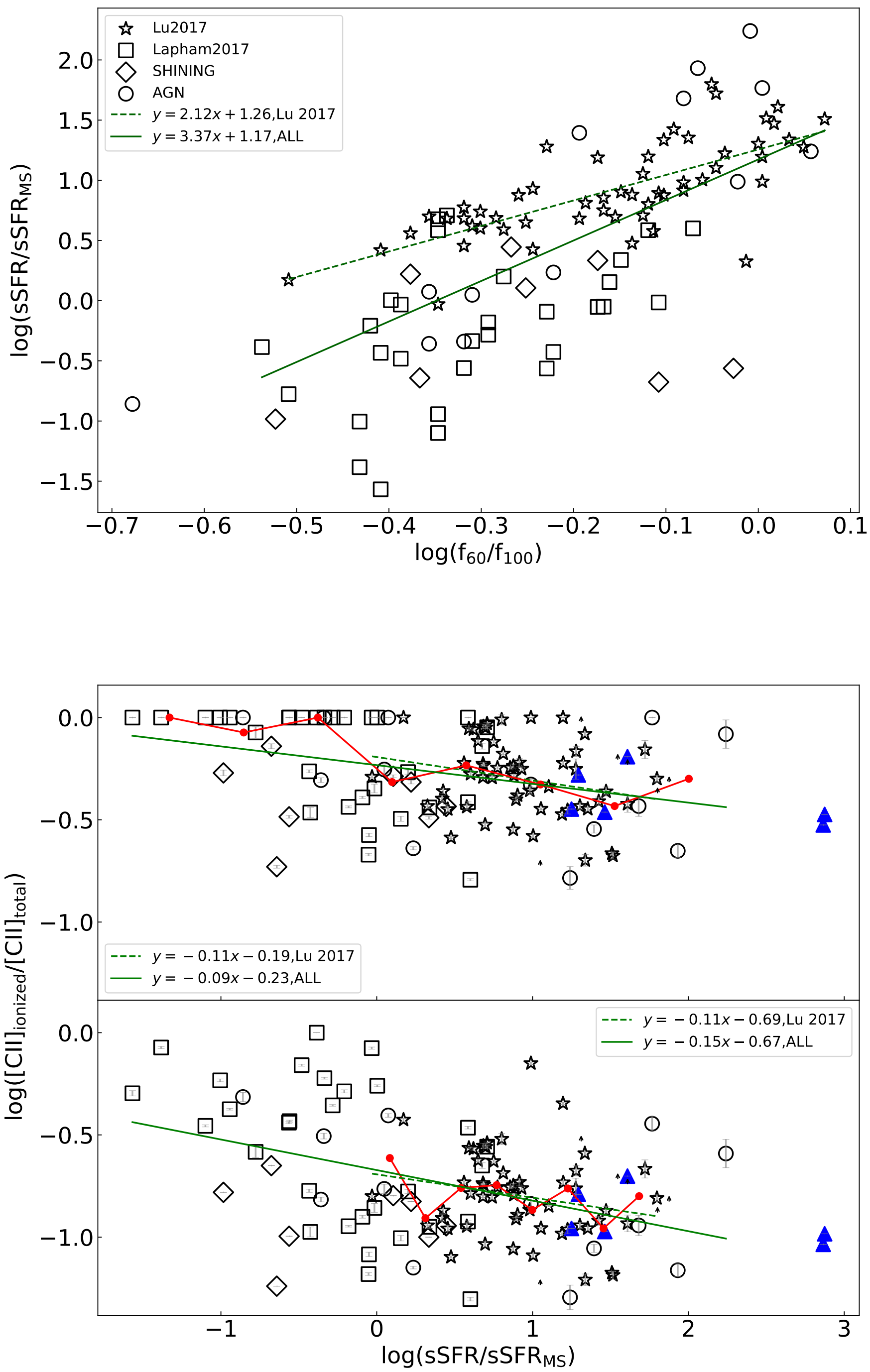

Figure 5. Top panel: The sSFR/$sSFR_{MS}$ vs. FIR color calculated by f_{60}/f_{100} for individual galaxies in our sample. The dashed green line represents the linear fit for the GOALS sample, while the solid line corresponds to the fit for the total sample. Bottom panel: $[C\ II]_{ionized}/[C\ II]_{total}$ vs. sSFR/$sSFR_{MS}$. All values are shown on a logarithmic scale. The signs are the same as Figure 2, and the blue filled triangles represent high-z galaxies. In the bottom panel, the upper panel shows the $[C\ II]_{ionized}/[C\ II]_{total}$ derived by log(C/N) = 0.75, while the lower panel corresponds to log(C/N) = 0.24. The red points and lines in the upper and lower panels represent the median values in each f_{60}/f_{100} bin for the total sample and (U)LIRGs, respectively.

encompasses a wider range for the GOALS and the total sample. The Spearman coefficients and p-values are −0.439 and 0.0008 for GOALS, and −0.493 and 3.88×10^{-6} for the total sample. The Kendall's τ and p-value are −0.47 and 2.69×10^{-4} for GOALS, and −0.51 and 1.22×10^{-6} for the total sample. These findings suggest a moderate negative correlation between $[C\ II]_{ionized}/[C\ II]_{total}$ and [O III]88 μm/[N II] 122 μm, which is stronger than Δ(MS).

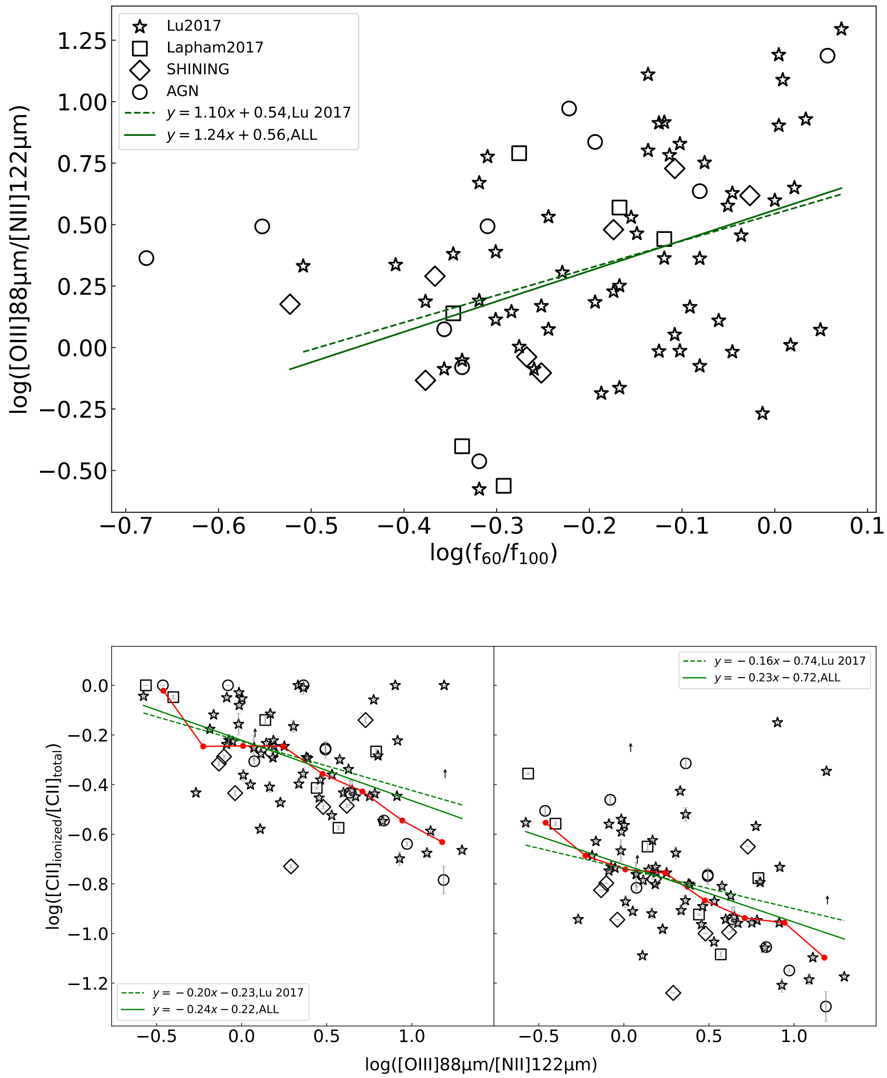

Figure 6. Top panel: The [O III]88 μm/[N II] 122 μm vs. FIR color for our sample. Bottom panel: log([C II]$_{\rm ionized}$/ [C II]$_{\rm total}$) vs. [O III]88 μm/[N II] 122 μm. Symbols are the same as Figure 4.

However, it is important to note that the [O III]88 μm/[N II] 122 μm ratio is not only sensitive to the hardness of the radiation field, but also correlates with the ionization parameter U under a fixed radiation hardness (Cormier et al. 2015; Zhao et al. 2016a). Since the FIR color is closely related to U (Abel et al. 2009; Fischer et al. 2014; Cormier et al. 2015; Zhao et al. 2016a), variations in [O III]88 μm/[N II] 122 μm may partly reflect changes in the ionization parameter. Díaz-Santos et al. (2017) showed that [O III]88 μm/[N II] 122 μm ratio probes mostly another ionization parameter q for starbursts with ages of a few Myr.

U can trace the galaxies hosting young stellar populations and experiencing high excitation conditions (e.g., Feltre et al. 2016; Gutkin et al. 2016; Jaskot & Ravindranath 2016; Micheva et al. 2020). Although the physical mechanisms of the [C III] emission are currently not well understood, galaxies with high U are expected to enhance the generation of [C III]. The observations of young, low-mass, low-metallicity galaxies have supported this finding (e.g., Erb et al. 2010; Stark et al. 2014, 2015; Berg et al. 2016; Maseda et al. 2017; Stark et al. 2017; Senchyna et al. 2017; Nakajima et al. 2018). As shown in Figure 5 of Berg et al. (2019), the ionization fraction of the C^{+} decreases with increasing log U, which suggests that more [C II] in the H II region may be ionized to the next ionization state, C^{++}. This would result in a decrease in the [C II]$_{\rm ionized}$/[C II]$_{\rm total}$.

Moreover, the [O III]88 μm/[N II] 122 μm ratio is also influenced by the nitrogen-to-oxygen abundance ratio (N/O). Pérez-Montero (2014) showed that N/O increases with metallicity (12+log(O/H)). Berg et al. (2019) found that

$\log(N/O) \sim -1.0$ at $12+\log(O/H) = 8.25$ rises to $\log(N/O) \sim -0.8$ at $12+\log(O/H) = 8.75$. In our sample, the metallicity spans $12 + \log(O/H) = 8.3$–8.9, consistent with the range covered in these studies. Zhang et al. (2018) reported that adopting H II region abundances from Savage & Sembach (1996) (with $\log(N/O) = -0.88$) yields [O III] 88 μm/[N II] 122 μm ratio approximately 1.15 × higher than that derived from Rubin (1985), whose $\log(N/O) = -0.77$. Meanwhile, the simulation by Díaz-Santos et al. (2017) demonstrated a factor of ∼2.5× decrease in [O III]88 μm/[N II] 122 μm ratio when metallicity increases from 1 $Z_\odot$ to 2 $Z_\odot$ ($Z_\odot$: $12+\log(O/H) = 8.69$; Asplund et al. 2009). In our sample, the observed [O III]88 μm/[N II] 122 μm span 0.3–10, exceeding the scale attributable solely to N/O abundance effects, suggesting that U remains the dominant driver. We will further explore the impact of metallicity on $[\mathrm{C\,II}]_{\mathrm{ionized}}/[\mathrm{C\,II}]_{\mathrm{total}}$ in the following section.

3.4. The Effect of Metallicity

In dwarf galaxies, Cormier et al. (2015) found that the radiation field is stronger in low-metallicity galaxies, while $[\mathrm{C\,II}]_{\mathrm{ionized}}/[\mathrm{C\,II}]_{\mathrm{total}}$ is low in these galaxies. Similarly, Maseda et al. (2017) have demonstrated a negative correlation between the strength of [C III] and the metallicity in low-metallicity galaxies. To further explore the relationship between $[\mathrm{C\,II}]_{\mathrm{ionized}}/[\mathrm{C\,II}]_{\mathrm{total}}$ and 12+log(O/H), we utilize the total 75 metallicity measurements collected in Section 2.

The Spearman correlation coefficients and p-values between $[\mathrm{C\,II}]_{\mathrm{ionized}}/[\mathrm{C\,II}]_{\mathrm{total}}$ and 12+log(O/H) for GOALS and total samples are (0.336,0.06) and (0.388,0.0006), respectively. Kendall's τ and p-values are (0.21,0.08) and (0.28,0.0006), respectively. These results indicate a moderate positive correlation between $[\mathrm{C\,II}]_{\mathrm{ionized}}/[\mathrm{C\,II}]_{\mathrm{total}}$ and 12+log(O/H). This trend is consistent with findings of Croxall et al. (2017), who found a clear decrease in observed [C II]/[N II] 205 μm ratio with increasing metallicity, suggesting that $[\mathrm{C\,II}]_{\mathrm{ionized}}/[\mathrm{C\,II}]_{\mathrm{total}}$ increases as metallicity rises. The median $[\mathrm{C\,II}]_{\mathrm{ionized}}/[\mathrm{C\,II}]_{\mathrm{total}}$ demonstrates an increasing trend with increasing metallicity. However, an inflection point is evident at $12 + \log(O/H) = 8.5 \sim 8.6$. This turning point is also apparent at this position when using the *locfit* function in R to fit as shown in Figure 7. One possible explanation is the significant increase in log(C/N) from $12 + \log(O/H) > 8.5 \sim 8.6$, as reported by Berg et al. (2019). It is noteworthy that our calculations adopt a uniform log(C/N) of 0.75, which may result in an underestimation of the $[\mathrm{C\,II}]_{\mathrm{ionized}}/[\mathrm{C\,II}]_{\mathrm{total}}$.

According to Senchyna et al. (2017), galaxies with oxygen abundance approximately $12 + \log \mathrm{O/H} \sim 7.7$ (Berg et al. 2016) to ∼8.5 show strong [C III] detections. The strength of [C III] significantly decreases in more metal-rich galaxies because of efficient cooling or in metal-poor galaxies due to the low carbon abundance (Micheva et al. 2020). Therefore, for the sample with metallicity below 8.5, the $[\mathrm{C\,II}]_{\mathrm{ionized}}/[\mathrm{C\,II}]_{\mathrm{total}}$ may be affected by metallicity due to its strong [C III] emission.

Nevertheless, it is important to acknowledge the limitations of the present study, including the relatively small sample size and the potential inaccuracies in metallicity calibration for AGNs. Future research could explore this domain by expanding the sample and considering more reliable metallicity calibrators to improve understanding of this correlation.

3.5. Does Molecular Gas Influence the $[\mathrm{C\,II}]_{\mathrm{ionized}}/[\mathrm{C\,II}]_{\mathrm{total}}$?

A strong correlation between SF activity and molecular gas has been established by Kennicutt (1998), Liu et al. (2015), Saintonge et al. (2016), and Accurso et al. (2017). Additionally, Berg et al. (2019) found that galaxies with higher star formation efficiency exhibit elevated log(C/N) values. Since the $[\mathrm{C\,II}]_{\mathrm{ionized}}/[\mathrm{C\,II}]_{\mathrm{total}}$ is influenced by both the electron density and log(C/N), it is pertinent to explore the relationship between molecular gas content and the $[\mathrm{C\,II}]_{\mathrm{ionized}}/[\mathrm{C\,II}]_{\mathrm{total}}$. To investigate this relationship, we plot molecular gas mass as a function of $[\mathrm{C\,II}]_{\mathrm{ionized}}/[\mathrm{C\,II}]_{\mathrm{total}}$, as shown in Figure 8.

We calculate the molecular gas mass ($M_{\mathrm{H_2}}$) from CO(1-0) luminosity ($L'_{\mathrm{CO(1-0)}}$) using the expression provided by Dickman et al. (1986) and Obreschkow & Rawlings (2009):

$$M_{\mathrm{H_2}} = \alpha_{\mathrm{CO}} L'_{\mathrm{CO(1-0)}} \tag{3}$$

Here, $M_{\mathrm{H_2}}$ is expressed in solar mass ($M_\odot$). The CO(1-0) luminosity, $L'_{\mathrm{CO}}(1-0)$, in units of K km s^{-1} pc^2, is related to the observed velocity integrated flux density, following Solomon et al. (1997):

$$L'_{\mathrm{CO(1-0)}} = 3.25 \times 10^7 I_{\mathrm{CO}} \Delta v \nu_{\mathrm{obs}}^{-2} D_{\mathrm{L}}^2 (1 + z)^{-3} \tag{4}$$

In this equation, ν_{obs} is the observed frequency in GHz, D_{L} is the luminosity distance in Mpc and $I_{\mathrm{CO}}\Delta v$ is the integrated line luminosity in Jy kms^{-1}. The factor α_{CO} is the CO-to-H2 conversion factor. The empirical CO(1–0) conversion factor for the Milky Way is typically 4.36 $M_\odot$ (K km s^{-1})$^{-1}$, which includes a 36% correction for helium gas (Strong & Mattox 1996; Abdo et al. 2010; Sandstrom et al. 2013). We adopt the conversion factor α_{CO} of 4.0 $M_\odot$ (K km s^{-1})$^{-1}$ for (U)LIRGs, 4.7 $M_\odot$ (K km s^{-1})$^{-1}$ for ETG, KINGFISH, and SHINING galaxies, and 4.8 $M_\odot$ (K km s^{-1})$^{-1}$ for AGNs, including helium contributions (see Table 7 in Dunne et al. 2022).

The red dots and line in the bottom panel of Figure 8 represent the median [C II]ionized/[C II]total in $M_{\mathrm{H_2}}$ bins for GOALS (with the last two bins combined due to the small sample size). Almost all (U)LIRGs in our sample have a molecular gas mass greater than $10^{9.5} M_\odot$. The lack of correlation between molecular gas and [C II]ionized/[C II]total may be attributed to a bias in the GOALS sample. Among the total sample, four sources, NGC 4151, NGC 2976, IC 342 and

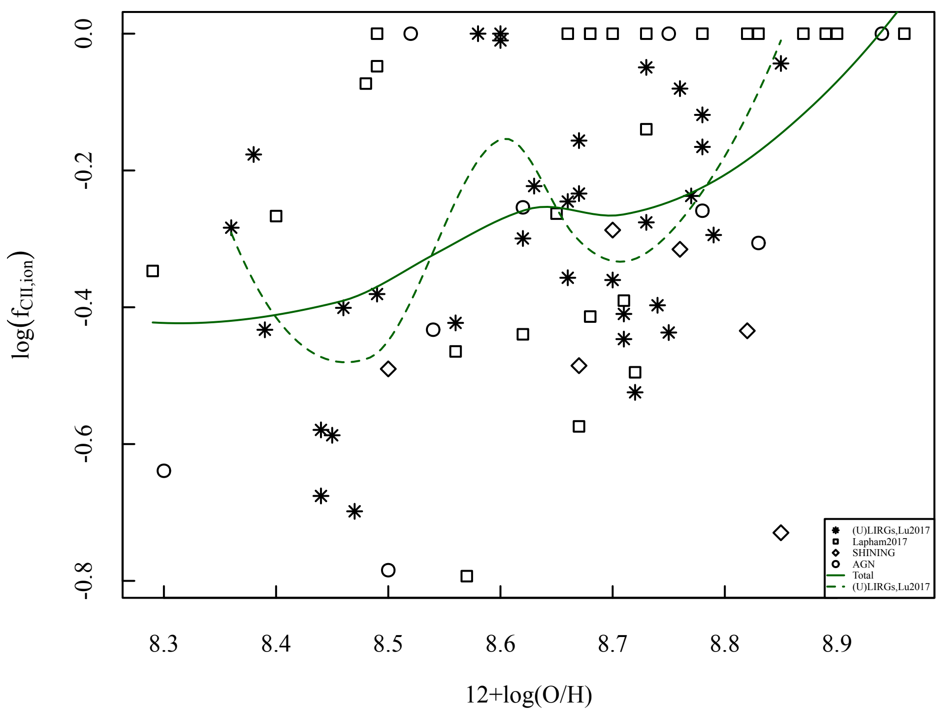

Figure 7. log($[C\ II]_{ionized}/[C\ II]_{total}$) vs. 12+log(O/H). Asterisks represent the (U)LIRGs in the samples of Lu et al. (2017a) and Díaz-Santos et al. (2017), while squares, diamonds, and circles represent ETG+KINGFISH, SHINING, and AGN samples, respectively. The green solid line indicates the best-fit to the total sample using *locfit* function in R. The dashed line represents the corresponding fit for the GOALS sample.

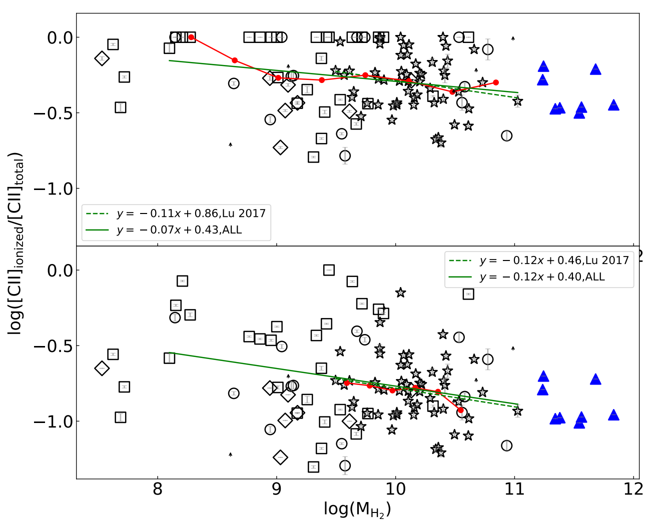

Figure 8. log($[C\ II]_{ionized}/[C\ II]_{total}$) vs. log($M_{H_2}$). The signs are the same as in the bottom panel of Figure 5.

NGC 3077, have molecular gas masses less than $10^{8.0}\,M_\odot$. CO emission is known to be deficient in low-metallicity galaxies (e.g., Indebetouw et al. 2013; Lebouteiller et al. 2017; Vallini et al. 2017; Jameson et al. 2018; Chevance et al. 2020; Wolfire et al. 2022). Madden et al. (2020) estimate that more than 70% of molecular gas is not traced by CO(1-0) in the DGS. The 12 + log(O/H) values for NGC 4151 and IC 342 are 8.34 and 8.49, respectively, suggesting that the molecular gas masses in these galaxies may be underestimated. Accurso et al. (2017) found that galaxies with stellar masses $<10^{10}\,M_\odot$ (for NGC 2976, $M_\star = 10^{10.5}\,M_\odot$; for NGC 3077, $M_\star = 10^{9.054} M_\odot$) exhibit significantly lower CO luminosities due to CO photodissociation effects. However, even after removing these four points, no clear correlation is observed ((ρ, p) = (−0.177, 0.07) for GOALS, (ρ, p) = (−0.173, 0.2) for the total sample), and only a slightly downward trend is visible in Figure 8. High-redshift galaxies (represented by blue filled triangles in Figure 8) also follow this trend. The α_{CO} values for high-redshift galaxies are the same as those for (U)LIRGs.

3.6. Can $[C\ II]_{neutral}$ Trace SFR and M_{H_2} Well?

Star formation predominantly occurs within neutral ISM, rendering the $[C\ II]_{neutral}$ a more reliable tracer of both SFR and M_{H_2} compared to $[C\ II]_{total}$. We study the relationship between $[C\ II]_{neutral}$ and $L_{CO(1-0)}$ as shown in Figure 9 to compare with the result presented in Zhao et al. (2024), whose [C II] is not separated. Although there is a moderate positive correlation between $[C\ II]_{neutral}$ and $L_{CO(1-0)}$, the rms deviation is 0.42 dex, which is higher than Zhao et al. (2024) (0.28 dex for their whole sample). This is mainly due to the fact that in galaxies with high $[C\ II]_{ionized}$, the $L_{[C\ II]_{total}}/L_{CO(1-0)}$ is low, and there is too little [C II] emission from neutral gas as

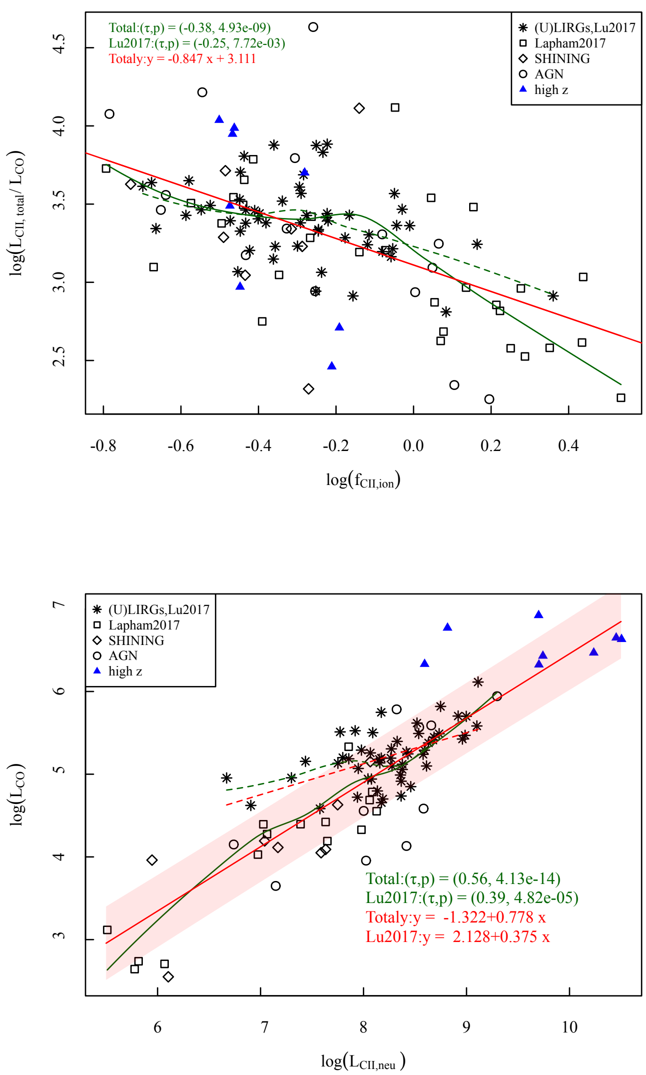

Figure 9. Top panel: $\log(L_{[\mathrm{C\,II}],\mathrm{total}}/L_{\mathrm{CO}})$ vs. $\log(f_{[\mathrm{C\,II}],\mathrm{ion}})$. Bottom panel: $\log(L_{\mathrm{CO}(1-0)})$ vs. $\log(L_{[\mathrm{C\,II}],\mathrm{neutral}})$. The signs are the same as Figure 7. High-redshift galaxies are marked with blue filled triangles. The red solid and dashed lines show the linear fit for the total and GOALS samples, respectively, with the red shaded region indicating the 1σ confidence interval of the total sample fit. The equation and Kendall's coefficients are annotated in the corner.

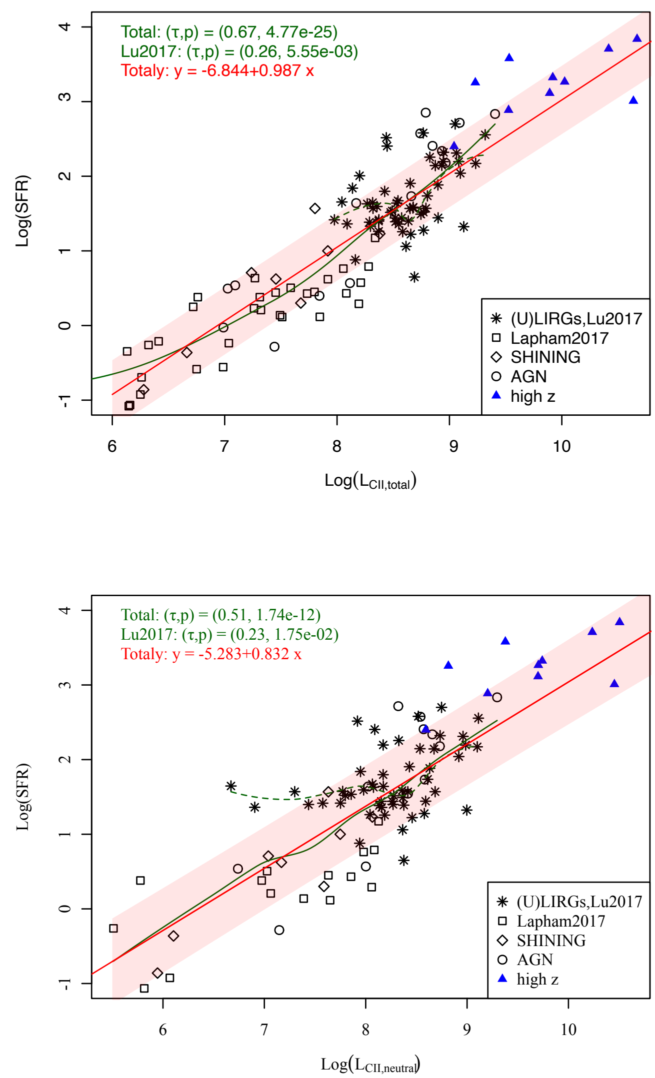

Figure 10. Top panel: SFR vs. $\log(L_{[\mathrm{C\,II}],\mathrm{total}})$. Bottom panel: SFR vs. $\log(L_{[\mathrm{C\,II}],\mathrm{neutral}})$. The signs are the same as Figure 9. The equation and Kendall's coefficients are annotated in the corner.

displayed in the top panel of Figure 9. Additionally, we include high-redshift ($z > 4$) galaxies (blue triangles) with both [C II], CO, and [N II] 205 μm detections (two sources only have 3σ upper limits on [N II] 205 μm emission), and adopt [N II] 122 μm/[N II] 205 μm of 2.2, based on a median value of our sample. Five of these high-redshift systems reside within the correlation's 1σ confidence interval. $[\mathrm{C\,II}]_{\mathrm{ionized}}$ is low in high-z galaxies, and $[\mathrm{C\,II}]_{\mathrm{neutral}}$ may be a reliable tracer for molecular gas mass when an appropriate [N II] 122 μm/[N II] 205 μm ratio is adopted. However, compared to $[\mathrm{C\,II}]_{\mathrm{total}}$, $[\mathrm{C\,II}]_{\mathrm{neutral}}$ is not a better tracer for molecular gas mass.

We further explore the relationship of $[\mathrm{C\,II}]_{\mathrm{neutral}}$–SFR and $[\mathrm{C\,II}]_{\mathrm{total}}$–SFR relations as shown in Figure 10, comparing the results with those from Sutter et al. (2019). The slope and scatter of $[\mathrm{C\,II}]_{\mathrm{total}}$–SFR (slope $= 0.987$, rms $= 0.44$ dex) are consistent with the findings of De Looze et al. (2014). While a positive correlation exists between $[\mathrm{C\,II}]_{\mathrm{neutral}}$ and SFR (Kendall's $\tau = 0.51$, $p = 1.74 \times 10^{-12}$), the scatter (rms $= 0.54$ dex) significantly exceeds that reported by Sutter et al. (2019) (0.23 dex), and the slope (0.832) is shallower. The higher scatter likely results from limited sampling at $\log([\mathrm{C\,II}]_{\mathrm{neutral}}) < 7$, where the small number of data points leads to increased statistical uncertainty. Our analysis incorporates high-redshift systems (blue triangles) with [C II], SFR, and [N II] 205 μm measurements, adopting our local sample's median [N II] 122 μm/[N II] 205 μm ratio (2.2).

Notably, eight high-redshift galaxies fall within the 1σ confidence interval of the [C II]$_{\rm neutral}$–SFR relation. This finding indicates that [C II]$_{\rm neutral}$–SFR may be suitable for high-z galaxies. In comparison to the [C II]$_{\rm total}$–FR relation for the total sample (Kendall's τ and p are 0.67 and 4.77 $\times$ 10^{-25}, respectively), [C II]$_{\rm neutral}$ shows a weaker correlation with SFR, characterized by greater scatter and a noticeable deviation from linearity, as shown in Figure 10. Therefore, [C II]$_{\rm neutral}$ does not trace the SFR well.

4. Conclusions

We utilize FIR emission line observations to ascertain the [C II]$_{\rm ionized}$/[C II]$_{\rm total}$ relative to the galaxy FIR color f_{60}/f_{100} for a sample of galaxies, including GOALS, ETGs, KINGFISH, SHININGs, and AGNs. The fraction of [C II] 158 μm from the ionized gas was recalculated using a revised carbon-to-nitrogen abundance ratio. Based on the emission line ratios, we investigated the correlation between the new [C II]$_{\rm ionized}$/[C II]$_{\rm total}$ and various galactic properties, including the environment and star formation activity. The conclusions derived from these analyses are as follows:

1. The electron density is derived from [N II] 122 μm/[N II] 205 μm. For the 108 total and 55 GOALS samples, the mean electron densities are 43 cm^{-3} and 44 cm^{-3}, respectively, with corresponding median values of 23 cm^{-3} and 32 cm^{-3}. Most of the derived densities fall within the range of 10–100 cm^{-3}. The corresponding [N II] 122 μm/[N II] 205 μm are 1.8, 1.27, and 1.53, respectively.
2. When adopting a log(C/N) of 0.75, the derived ionized-to-total [C II] ratio ([C II]$_{\rm ionized}$/[C II]$_{\rm total}$) is three times the previous value (log(C/N) = 0.24). The derived [C II]$_{\rm ionized}$/[C II]$_{\rm total}$ ratios for both adopted C/N values exhibit a declining trend with increasing FIR color, showing a moderate negative correlation for the total sample and the GOALS sample (Spearman coefficient, (ρ, p) = (−0.5, 2.8 $\times$ 10^{-8}) for the total sample, (ρ, p) = (–0.374, 0.005) for the GOALS sample).
3. For the GOALS subsample, no significant correlation is found between [C II]$_{\rm ionized}$/[C II]$_{\rm total}$ and Δ(MS), likely due to inherent biases in the Δ(MS) measurements within this particular sample. However, a weak negative correlation emerges when considering the total sample of 106 galaxies with both sSFR and stellar mass measurements (τ, p = −0.19, 0.004). This observed anticorrelation may be attributed to suppressed [C II] emission from H II regions in galaxies exhibiting enhanced star formation activity relative to the main sequence, possibly due to increased radiation field or ISM conditions.
4. The investigation focused on the GOALS and total samples reveals a stronger moderate negative correlation between [C II]$_{\rm ionized}$/[C II]$_{\rm total}$ and [O III]88 μm/[N II] 122 μm (for the total sample:ρ, p = −0.493, 3.88 $\times$ 10^{-6}; for GOALS: ρ, p = −0.439, 0.0008), which is notably stronger than the weak anticorrelation with Δ(MS). The [C II] in ionized gas may undergo further ionization, decreasing the [C II]$_{\rm ionized}$ in galaxies with active star formation.
5. A moderate positive correlation is found between the [C II]$_{\rm ionized}$/[C II]$_{\rm total}$ and metallicity for the 75 galaxies with metallicity measurements in Section 2. However, a notable decline in the [C II]$_{\rm ionized}$/[C II]$_{\rm total}$ at 12 + log(O/H) = 8.5 − 8.6 is evident. This decline is likely attributable to a substantial increase in log(C/N) starting at 12 + log(O/H) = 8.5 (Berg et al. 2019), which has not been considered in our calculations.
6. For both the GOALS sample and the total sample, we find no significant correlation between [C II]$_{\rm ionized}$/[C II]$_{\rm total}$ and molecular gas mass (for GOALS:(ρ, p) = (−0.177, 0.07); for the total sample: (ρ, p) = (–0.173, 0.2)), though there is a slightly downward trend with increasing molecular gas mass.
7. Our analysis reveals significant scatter in the $L_{\rm CO(1-0)} - L_{\rm [C\,II]_{neutral}}$ correlation (σ = 0.42 dex), exceeding the dispersion presented in the $L_{\rm CO(1-0)} - L_{\rm [C\,II]_{total}}$ relation reported by Zhao et al. (2024) (σ = 0.28 dex). This finding implies that the latter method may serve as a more reliable tracer of molecular gas mass in galaxies with elevated [C II]$_{\rm ionized}$/[C II]$_{\rm total}$. The combination of increased scatter and a shallower slope in the $L_{\rm [C\,II]_{neutral}}$ − SFR relation (Figure 10) underscores the limitations of [C II]$_{\rm neutral}$ as a standalone tracer of star formation in ionization-dominated systems.

Above all, we can tentatively attribute the variation of [C II]$_{\rm ionized}$/[C II]$_{\rm total}$ mainly to metallicity, star formation activity, and ionization parameters. The [C II]$_{\rm ionized}$/[C II]$_{\rm total}$ exhibits a negative correlation with the intensity of star formation activity and the magnitude of the ionization parameter. Additionally, an increase in metallicity may lead to a decrease in the [C III] emission and an increase in [C II]$_{\rm ionized}$/[C II]$_{\rm total}$.

Acknowledgments

We thank the anonymous referee for useful comments/suggestions that helped us to improve the manuscript. This work is supported by the National Natural Science Foundation of China (NSFC, grant No. 12173079). This research uses the NASA/IPAC Extragalactic Database (NED), which is operated by the Jet Propulsion Laboratory, California Institute of Technology, under contract with the National Aeronautics and Space Administration. PACS has been developed by a consortium of institutes led by MPE (Germany) and including UVIE (Austria); KU Leuven, CSL, IMEC (Belgium); CEA, LAM (France); MPIA (Germany); INAF-IFSI/OAA/OAP/OAT, LENS, SISSA (Italy); and IAC (Spain). This development has been supported by the funding agencies BMVIT (Austria), ESA-PRODEX (Belgium), CEA/CNES (France), DLR (Germany), ASI/INAF (Italy), and CICYT/MCYT

(Spain). SPIRE has been developed by a consortium of institutes led by Cardiff University (UK) and including Univ. Lethbridge (Canada); NAOC (China); CEA, LAM (France); IFSI, Univ. Padua (Italy); IAC (Spain); Stockholm Observatory (Sweden); Imperial College London, RAL, UCL-MSSL, UKATC, Univ. Sussex (UK); and Caltech, JPL, NHSC, Univ. Colorado (USA). This development has been supported by national funding agencies: CSA (Canada); NAOC (China); CEA, CNES, CNRS (France); ASI (Italy); MCINN (Spain); SNSB (Sweden); STFC and UKSA (UK); and NASA (USA). HIPE is a joint development by the Herschel Science Ground Segment Consortium, consisting of ESA, the NASA Herschel Science Center, and the HIFI, PACS, and SPIRE consortia. Based on observations collected at the Centro Astronómico Hispano Alemán (CAHA) at Calar Alto, operated jointly by the Max-Planck Institut für Astronomie and the Instituto de Astrofìsica de Andalucìa (CSIC). The Spitzer Space Telescope is operated by the Jet Propulsion Laboratory, California Institute of Technology, under NASA contract 1407.

ORCID iDs

Jiamin Liu https://orcid.org/0009-0003-6261-0824
Yinghe Zhao (赵应和) https://orcid.org/0000-0002-9128-818X

References

Abdo, A. A., Ackermann, M., Ajello, M., et al. 2010, ApJ, 710, 133
Abel, N. P., Dudley, C., Fischer, J., Satyapal, S., & van Hoof, P. A. M. 2009, ApJ, 701, 1147
Abel, N. P., Ferland, G. J., Shaw, G., & van Hoof, P. A. M. 2005, ApJS, 161, 65
Accurso, G., Saintonge, A., Catinella, B., et al. 2017, MNRAS, 470, 4750
Alatalo, K., Davis, T. A., Bureau, M., et al. 2013, MNRAS, 432, 1796
Alatalo, K., Petric, A. O., Lanz, L., et al. 2024, ApJ, 975, 241
Albrecht, M., Chini, R., Krügel, E., Müller, S. A. H., & Lemke, R. 2004, A&A, 414, 141
Ali, I. A. M., Hwang, C.-Y., & Lemke, R. 2018, JFAS, 11, 632
Alonso-Herrero, A., Pereira-Santaella, M., Rieke, G. H., & Rigopoulou, D. 2012, ApJ, 744, 2
Armus, L., Charmandaris, V., Bernard-Salas, J., et al. 2007, ApJ, 656, 148
Armus, L., Mazzarella, J. M., Evans, A. S., et al. 2009, PASP, 121, 559
Asplund, M., Grevesse, N., Sauval, A. J., & Scott, P. 2009, ARA&A, 47, 481
Baan, W. A., Henkel, C., Loenen, A. F., Baudry, A., & Wiklind, T. 2008, A&A, 477, 747
Ballesteros-Paredes, J., Klessen, R. S., Mac Low, M. M., & Vazquez-Semadeni, E. 2007, in Protostars and Planets V, ed. B. Reipurth, D. Jewitt, & K. Keil, 63
Bell, E. F., McIntosh, D. H., Katz, N., & Weinberg, M. D. 2003, ApJS, 149, 289
Berg, D. A., Erb, D. K., Henry, R. B. C., Skillman, E. D., & McQuinn, K. B. W. 2019, ApJ, 874, 93
Berg, D. A., Skillman, E. D., Henry, R. B. C., Erb, D. K., & Carigi, L. 2016, ApJ, 827, 126
Berta, S., Magnelli, B., Nordon, R., et al. 2011, A&A, 532, A49
Bottorff, M., Lamothe, J., Momjian, E., et al. 1998, PASP, 110, 1040
Bouwens, R. J., Smit, R., Schouws, S., et al. 2022, ApJ, 931, 160
Brauher, J. R., Dale, D. A., & Helou, G. 2008, ApJS, 178, 280
Cao, Y. 2018, PhD thesis, University of Illinois, Urbana-Champaign
Cappellari, M., Emsellem, E., Krajnović, D., et al. 2011, MNRAS, 413, 813
Caputi, K. I., Lagache, G., Yan, L., et al. 2007, ApJ, 660, 97
Carilli, C. L., & Walter, F. 2013, ARA&A, 51, 105
Carniani, S., Ferrara, A., Maiolino, R., et al. 2020, MNRAS, 499, 5136
Casasola, V., Bianchi, S., Magrini, L., et al. 2022, A&A, 668, A130
Cheng, C., Cao, X., Lu, N., et al. 2020, ApJ, 898, 33
Chevance, M., Madden, S. C., Fischer, C., et al. 2020, MNRAS, 494, 5279
Combes, F., Baker, A. J., Schinnerer, E., et al. 2009, A&A, 503, 73
Corbett, E. A., Kewley, L., Appleton, P. N., et al. 2003, ApJ, 583, 670
Cormier, D., Madden, S. C., Lebouteiller, V., et al. 2015, A&A, 578, A53
Crawford, M. K., Genzel, R., Townes, C. H., & Watson, D. M. 1985, ApJ, 291, 755
Croxall, K. V., Smith, J. D., Pellegrini, E., et al. 2017, ApJ, 845, 96
Cullen, F., McLure, R. J., Dunlop, J. S., et al. 2019, MNRAS, 487, 2038
Davis, T. A., Young, L. M., Crocker, A. F., et al. 2014, MNRAS, 444, 3427
De Looze, I., Cormier, D., Lebouteiller, V., et al. 2014, A&A, 568, A62
de los Reyes, M. A. C., & Kennicutt, R. C., Jr. 2019, ApJ, 872, 16
Desai, V., Armus, L., Spoon, H. W. W., et al. 2007, ApJ, 669, 810
Díaz-Santos, T., Armus, L., Charmandaris, V., et al. 2013, ApJ, 774, 68
Díaz-Santos, T., Armus, L., Charmandaris, V., et al. 2017, ApJ, 846, 32
Díaz-Santos, T., Charmandaris, V., Armus, L., et al. 2010, ApJ, 723, 993
Díaz-Santos, T., Charmandaris, V., Armus, L., et al. 2011, ApJ, 741, 32
Dickman, R. L., Snell, R. L., & Schloerb, F. P. 1986, ApJ, 309, 326
Dors, O. L., Cardaci, M. V., Hägele, G. F., et al. 2015, MNRAS, 453, 4102
Draine, B. T. 2011, ApJ, 732, 100
Dunne, L., Maddox, S. J., Papadopoulos, P. P., Ivison, R. J., & Gomez, H. L. 2022, MNRAS, 517, 962
Dye, S., Eales, S. A., Gomez, H. L., et al. 2022, MNRAS, 510, 3734
Elmegreen, B. G. 2007, ApJ, 668, 1064
Elmegreen, B. G., & Burkert, A. 2010, ApJ, 712, 294
Elmegreen, B. G., & Scalo, J. 2004, ARA&A, 42, 211
Erb, D. K., Pettini, M., Shapley, A. E., et al. 2010, ApJ, 719, 1168
Esposito, F., Vallini, L., Pozzi, F., et al. 2022, MNRAS, 512, 686
Evans, A. S., Mazzarella, J. M., Surace, J. A., & Sanders, D. B. 2002, ApJ, 580, 749
Farrah, D., Efstathiou, A., Afonso, J., et al. 2022, MNRAS, 513, 4770
Feltre, A., Charlot, S., & Gutkin, J. 2016, MNRAS, 456, 3354
Ferkinhoff, C., Brisbin, D., Nikola, T., et al. 2011, ApJL, 740, L29
Fernández-Ontiveros, J. A., Pérez-Montero, E., Vílchez, J. M., Amorín, R., & Spinoglio, L. 2021, A&A, 652, A23
Fernández-Ontiveros, J. A., Spinoglio, L., Pereira-Santaella, M., et al. 2016, ApJS, 226, 19
Ferrière, K. M. 2001, RvMP, 73, 1031
Fischer, J., Abel, N. P., González-Alfonso, E., et al. 2014, ApJ, 795, 117
Gao, Y., Gu, Q., Shi, Y., et al. 2022, A&A, 661, A136
George, K., Joseph, P., Mondal, C., et al. 2019, A&A, 621, L4
Gilli, R., Norman, C., Vignali, C., et al. 2014, A&A, 562, A67
Goldsmith, P. F., Langer, W. D., Pineda, J. L., & Velusamy, T. 2012, ApJS, 203, 13
Goldsmith, P. F., Yıldız, U. A., Langer, W. D., & Pineda, J. L. 2015, ApJ, 814, 133
González-Alfonso, E., Fischer, J., Sturm, E., et al. 2015, ApJ, 800, 69
Graham, A. W., Jarrett, T. H., & Cluver, M. E. 2024, MNRAS, 527, 10059
Gutkin, J., Charlot, S., & Bruzual, G. 2016, MNRAS, 462, 1757
Haan, S., Surace, J. A., Armus, L., et al. 2011, AJ, 141, 100
Heiles, C. 1994, ApJ, 436, 720
Helfer, T. T., Thornley, M. D., Regan, M. W., et al. 2003, ApJS, 145, 259
Herrera-Camus, R., Sturm, E., Graciá-Carpio, J., et al. 2018a, ApJ, 861, 94
Herrera-Camus, R., Sturm, E., & Graciá-Carpio, J. 2018b, ApJ, 861, 95
Herrero-Illana, R., Privon, G. C., Evans, A. S., et al. 2019, A&A, 628, A71
Hollenbach, D. J., & Tielens, A. G. G. M. 1999, RvMP, 71, 173
Hopkins, P. F., Hernquist, L., Cox, T. J., & Kereš, D. 2008, ApJS, 175, 356
Howell, J. H., Armus, L., Mazzarella, J. M., et al. 2010, ApJ, 715, 572
Inami, H., Armus, L., Charmandaris, V., et al. 2013, ApJ, 777, 156
Indebetouw, R., Brogan, C., Chen, C. H. R., et al. 2013, ApJ, 774, 73
Iwasawa, K., Sanders, D. B., Teng, S. H., et al. 2011, A&A, 529, A106
Jameson, K. E., Bolatto, A. D., Wolfire, M., et al. 2018, ApJ, 853, 111
Jaskot, A. E., & Ravindranath, S. 2016, ApJ, 833, 136
Jiao, Q., Zhao, Y., Zhu, M., et al. 2017, ApJL, 840, L18
Jones, G. C., Maiolino, R., Caselli, P., & Carniani, S. 2020, MNRAS, 498, 4109
Joung, M. R., Mac Low, M.-M., & Bryan, G. L. 2009, ApJ, 704, 137
Kamenetzky, J., Rangwala, N., Glenn, J., Maloney, P. R., & Conley, A. 2014, ApJ, 795, 174
Kamenetzky, J., Rangwala, N., Glenn, J., Maloney, P. R., & Conley, A. 2016, ApJ, 829, 93

Kang, X., Chang, R., Zhang, F., Cheng, L., & Wang, L. 2015, MNRAS, 449, 414
Kaufman, M. J., Wolfire, M. G., Hollenbach, D. J., & Luhman, M. L. 1999, ApJ, 527, 795
Kennicutt, R. C., & Evans, N. J. 2012, ARA&A, 50, 531
Kennicutt, R. C., Jr. 1998, ApJ, 498, 541
Kennicutt, R. C., Jr., & De Los Reyes, M. A. C. 2021, ApJ, 908, 61
Kennicutt, R. C., Calzetti, D., Aniano, G., et al. 2011, PASP, 123, 1347
Kewley, L. J., & Ellison, S. L. 2008, ApJ, 681, 1183
Kewley, L. J., Heisler, C. A., Dopita, M. A., & Lumsden, S. 2001, ApJS, 132, 37
Kim, D. C., Evans, A. S., Vavilkin, T., et al. 2013, ApJ, 768, 102
Kohno, K., Ishizuki, S., Matsushita, S., Vila-Vilaró, B., & Kawabe, R. 2003, PASJ, 55, L1
Kritsuk, A. G., & Norman, M. L. 2002, ApJL, 569, L127
Kroupa, P. 2002, Sci, 295, 82
Kuno, N., Sato, N., Nakanishi, H., et al. 2007, PASJ, 59, 117
Lapham, R. C., Young, L. M., & Crocker, A. 2017, ApJ, 840, 51
Le Fèvre, O., Béthermin, M., Faisst, A., et al. 2020, A&A, 643, A1
Lebouteiller, V., Cormier, D., Madden, S. C., et al. 2019, A&A, 632, A106
Lebouteiller, V., Péquignot, D., Cormier, D., et al. 2017, A&A, 602, A45
Leroy, A. K., Walter, F., Brinks, E., et al. 2008, AJ, 136, 2782
Liu, L., Gao, Y., & Greve, T. R. 2015, ApJ, 805, 31
Lu, N., Zhao, Y., Díaz-Santos, T., et al. 2017a, ApJS, 230, 1
Lu, N., Zhao, Y., Díaz-Santos, T., et al. 2017b, ApJL, 842, L16
Luhman, M. L., Satyapal, S., Fischer, J., et al. 1998, ApJL, 504, L11
Ma, J., Gonzalez, A. H., Spilker, J. S., et al. 2015, ApJ, 812, 88
Madau, P., & Dickinson, M. 2014, ARA&A, 52, 415
Madden, S. C., Cormier, D., Hony, S., et al. 2020, A&A, 643, A141
Magnelli, B., Elbaz, D., Chary, R. R., et al. 2011, A&A, 528, A35
Magnelli, B., Lutz, D., Saintonge, A., et al. 2014, A&A, 561, A86
Malhotra, S., Helou, G., Stacey, G., et al. 1997, ApJL, 491, L27
Malhotra, S., Kaufman, M. J., Hollenbach, D., et al. 2001, ApJ, 561, 766
Maseda, M. V., Brinchmann, J., Franx, M., et al. 2017, A&A, 608, A4
Matsuki, Y., Koyama, Y., Nakagawa, T., & Takita, S. 2017, MNRAS, 466, 2517
McKee, C. F., & Ostriker, E. C. 2007, ARA&A, 45, 565
McKee, C. F., & Ostriker, J. P. 1977, ApJ, 218, 148
Meijerink, R. 2006, PhD thesis, University of Leiden, Netherlands
Menéndez-Delmestre, K., Blain, A. W., Smail, I., et al. 2009, ApJ, 699, 667
Micheva, G., Östlin, G., Melinder, J., et al. 2020, ApJ, 903, 123
Micheva, G., Roth, M. M., Weilbacher, P. M., et al. 2022, A&A, 668, A74
Montoya Arroyave, I., Cicone, C., Makroleivaditi, E., et al. 2023, A&A, 673, A13
Morokuma-Matsui, K., Sorai, K., Sato, Y., et al. 2020, PASJ, 72, 90
Moustakas, J., & Kennicutt, R. C., Jr. 2006, ApJS, 164, 81
Murphy, E. J., Stierwalt, S., Armus, L., Condon, J. J., & Evans, A. S. 2013, ApJ, 768, 2
Nakajima, K., Schaerer, D., Le Fèvre, O., et al. 2018, A&A, 612, A94
Nandi, P., & Subramonian Stalin, C. 2024, BSRSL, 93, 780
Oberst, T. E., Parshley, S. C., Stacey, G. J., et al. 2006, ApJL, 652, L125
Obreschkow, D., & Rawlings, S. 2009, MNRAS, 394, 1857
Okada, Y., Güsten, R., Requena-Torres, M. A., et al. 2019, A&A, 621, A62
Papadopoulos, P. P., Thi, W.-F., Miniati, F., & Viti, S. 2011, MNRAS, 414, 1705
Pérez-Díaz, B., Masegosa, J., Márquez, I., & Pérez-Montero, E. 2021, MNRAS, 505, 4289
Pérez-Díaz, B., Pérez-Montero, E., Fernández-Ontiveros, J. A., et al. 2024, A&A, 685, A168
Pérez-Montero, E. 2014, MNRAS, 441, 2663
Petric, A. O., Armus, L., Howell, J., et al. 2011, ApJ, 730, 28
Pettini, M., & Pagel, B. E. J. 2004, MNRAS, 348, L59
Pilbratt, G. L., Riedinger, J. R., Passvogel, T., et al. 2010, A&A, 518, L1
Pilyugin, L. S., Vílchez, J. M., & Contini, T. 2004, A&A, 425, 849
Pineda, J. L., Langer, W. D., & Goldsmith, P. F. 2014, A&A, 570, A121
Pineda, J. L., Langer, W. D., Velusamy, T., & Goldsmith, P. F. 2013, A&A, 554, A103
Pope, A., Chary, R.-R., Alexander, D. M., et al. 2008, ApJ, 675, 1171
Rémy-Ruyer, A., Madden, S. C., Galliano, F., et al. 2014, A&A, 563, A31
Rodighiero, G., Cimatti, A., Gruppioni, C., et al. 2010, A&A, 518, L25
Rubin, R. H. 1985, ApJS, 57, 349
Rupke, D. S. N., Veilleux, S., & Baker, A. J. 2008, ApJ, 674, 172
Saintonge, A., Catinella, B., Cortese, L., et al. 2016, MNRAS, 462, 1749
Salak, D., Hashimoto, T., Inoue, A. K., et al. 2024, ApJ, 962, 1
Sánchez-Menguiano, L., Sánchez, S. F., Pérez, I., et al. 2017, A&A, 603, A113
Sanders, D. B., & Mirabel, I. F. 1996, ARA&A, 34, 749
Sandstrom, K. M., Leroy, A. K., Walter, F., et al. 2013, ApJ, 777, 5
Sargsyan, L., Samsonyan, A., Lebouteiller, V., et al. 2014, ApJ, 790, 15
Savage, B. D., & Sembach, K. R. 1996, ARA&A, 34, 279
Seifried, D., Banerjee, R., Klessen, R. S., Duffin, D., & Pudritz, R. E. 2011, MNRAS, 417, 1054
Senchyna, P., Stark, D. P., Vidal-García, A., et al. 2017, MNRAS, 472, 2608
Sofue, Y., Koda, J., Nakanishi, H., & Hidaka, M. 2003, PASJ, 55, 75
Solomon, P. M., Downes, D., Radford, S. J. E., & Barrett, J. W. 1997, ApJ, 478, 144
Solomon, P. M., & Vanden Bout, P. A. 2005, ARA&A, 43, 677
Sorai, K., Kuno, N., Muraoka, K., et al. 2019, PASJ, 71, S14
Spilker, J. S., Marrone, D. P., Aravena, M., et al. 2016, ApJ, 826, 112
Spinoglio, L., Fernández-Ontiveros, J. A., Malkan, M. A., et al. 2022, ApJ, 926, 55
Stacey, G. J., Geis, N., Genzel, R., et al. 1991, ApJ, 373, 423
Stacey, G. J., Hailey-Dunsheath, S., Ferkinhoff, C., et al. 2010, ApJ, 724, 957
Stark, D. P., Ellis, R. S., Charlot, S., et al. 2017, MNRAS, 464, 469
Stark, D. P., Richard, J., Charlot, S., et al. 2015, MNRAS, 450, 1846
Stark, D. P., Richard, J., Siana, B., et al. 2014, MNRAS, 445, 3200
Stierwalt, S., Armus, L., Charmandaris, V., et al. 2014, ApJ, 790, 124
Stierwalt, S., Armus, L., Surace, J. A., et al. 2013, ApJS, 206, 1
Strong, A. W., & Mattox, J. R. 1996, A&A, 308, L21
Sturm, E., González-Alfonso, E., Veilleux, S., et al. 2011, ApJL, 733, L16
Sun, F., Helton, J. M., Egami, E., et al. 2024, ApJ, 961, 69
Sutter, J., Dale, D. A., Croxall, K. V., et al. 2019, ApJ, 886, 60
Tarantino, E., Bolatto, A. D., Herrera-Camus, R., et al. 2021, ApJ, 915, 92
Tielens, A. G. G. M., & Hollenbach, D. 1985a, ApJ, 291, 722
Tielens, A. G. G. M., & Hollenbach, D. 1985b, ApJ, 291, 747
Tripodi, R., Feruglio, C., Fiore, F., et al. 2022, A&A, 665, A107
Tsai, A.-L., Matsushita, S., Nakanishi, K., et al. 2009, PASJ, 61, 237
U, V., Sanders, D. B., Mazzarella, J. M., et al. 2012, ApJS, 203, 9
Uzgil, B. D., Oesch, P. A., Walter, F., et al. 2021, ApJ, 912, 67
Vallini, L., Ferrara, A., Pallottini, A., & Gallerani, S. 2017, MNRAS, 467, 1300
Vallini, L., Gallerani, S., Ferrara, A., Pallottini, A., & Yue, B. 2015, ApJ, 813, 36
van Dishoeck, E. F., & Black, J. H. 1988, ApJ, 334, 771
van Driel, W., van den Broek, A. C., & de Jong, T. 1991, A&AS, 90, 55
Veilleux, S., Rupke, D. S. N., Kim, D. C., et al. 2009, ApJS, 182, 628
Vinod, K. T., Baheeja, C., Aswathy, S., & Ravikumar, C. D. 2023, RAA, 23, 045008
Voit, G. M. 1992, ApJ, 399, 495
Walter, F., Weiß, A., Riechers, D. A., et al. 2009, ApJL, 691, L1
Weingartner, J. C., & Draine, B. T. 2001, ApJS, 134, 263
Whitaker, K. E., van Dokkum, P. G., Brammer, G., & Franx, M. 2012, ApJL, 754, L29
Wolfire, M. G., Hollenbach, D., McKee, C. F., Tielens, A. G. G. M., & Bakes, E. L. O. 1995, ApJ, 443, 152
Wolfire, M. G., McKee, C. F., Hollenbach, D., & Tielens, A. G. G. M. 2003, ApJ, 587, 278
Wolfire, M. G., Vallini, L., & Chevance, M. 2022, ARA&A, 60, 247
Wootten, A., & Thompson, A. R. 2009, IEEEP, 97, 1463
Wright, E. L., Mather, J. C., Bennett, C. L., et al. 1991, ApJ, 381, 200
Xia, X. Y., Gao, Y., Hao, C. N., et al. 2012, ApJ, 750, 92
Xu, C. K., Cao, C., Lu, N., et al. 2014, ApJ, 787, 48
Xu, C. K., Cao, C., Lu, N., et al. 2015, ApJ, 799, 11
Yamashita, T., Komugi, S., Matsuhara, H., et al. 2017, ApJ, 844, 96
Young, L. M., Bureau, M., & Cappellari, M. 2008, ApJ, 676, 317
Yun, M. S., Aretxaga, I., Gurwell, M. A., et al. 2015, MNRAS, 454, 3485
Zhang, Z.-Y., Ivison, R. J., George, R. D., et al. 2018, MNRAS, 481, 59
Zhao, Y., Liu, J., Zhang, Z.-Y., & Bisbas, T. G. 2024, ApJ, 977, 46
Zhao, Y., Lu, N., Xu, C. K., et al. 2013, ApJL, 765, L13
Zhao, Y., Lu, N., Xu, C. K., et al. 2016a, ApJ, 819, 69
Zhao, Y., Lu, N., Xu, C. K., et al. 2016b, ApJ, 820, 118
Zhao, Y., Yan, L., & Tsai, C.-W. 2016c, ApJ, 824, 146